### Title

Single-cell multi-modal integrative analyses highlight functional dynamic gene regulatory networks directing human cardiac development




### Journal

Cell Genomics, 4(11)

### ISSN

2666-979X



### Authors

Holman, Alyssa R

Tran, Shaina

Destici, Eugin

et al.



### Publication Date

2024-11-01

### DOI

10.1016/j.xgen.2024.100680

Peer reviewed

Cell Genomics

Article

# Single-cell multi-modal integrative analyses highlight functional dynamic gene regulatory networks directing human cardiac development

## Graphical abstract

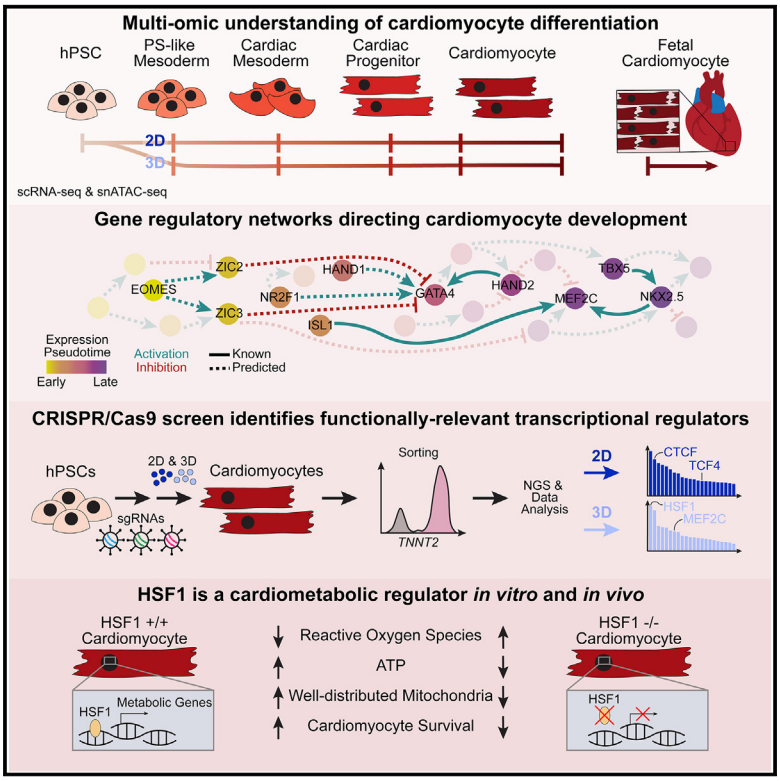


## Highlights

- Defined gene networks directing distinct human cardiomyocyte developmental stages
- Revealed divergent cardiomyocyte lineages with distinct gene programs and functions
- Uncovered key transcription factors for lineage-specific cardiomyocyte traits
- Linked HSF1 loss to impaired cardiac metabolism and survival in human cells

## Authors

Alyssa R. Holman, Shaina Tran, Eugin Destici, ..., Aileena C. Nelson, Adam J. Engler, Neil C. Chi

## Correspondence

nchi@health.ucsd.edu

## In brief

Holman et al. uncover distinct genetic programs driving human cardiomyocyte development, demonstrating how different developmental gene regulatory pathways lead to functional differences in cardiac cells. Their findings identify key transcription factors, including HSF1, which plays a critical role in cardiac metabolism and cell survival, offering insights into regenerative therapies for heart disease.

Holman et al., 2024, Cell Genomics *4*, 100680
November 13, 2024 
https://doi.org/10.1016/j.xgen.2024.100680

CellPress

Cell Genomics

CellPress
OPEN ACCESS

Article

# Single-cell multi-modal integrative analyses highlight functional dynamic gene regulatory networks directing human cardiac development

Alyssa R. Holman,[1,2] Shaina Tran,[1] Eugin Destici,[1] Elie N. Farah,[1] Ting Li,[1] Aileena C. Nelson,[1,3] Adam J. Engler,[3,4,5] and Neil C. Chi[1,3,4,6,7,*]

[1]Division of Cardiology, Department of Medicine, University of California, San Diego, La Jolla, CA 92093, USA
[2]Biomedical Sciences Graduate Program, University of California, San Diego, La Jolla, CA 92093, USA
[3]Department of Bioengineering, University of California, San Diego, La Jolla, CA 92093, USA
[4]Institute of Engineering Medicine, University of California, San Diego, La Jolla, CA 92093, USA
[5]Sanford Consortium for Regenerative Medicine, La Jolla, CA 92093, USA
[6]Institute of Genomic Medicine, University of California, San Diego, La Jolla, CA 92093, USA
[7]Lead contact
*Correspondence: nchi@health.ucsd.edu
https://doi.org/10.1016/j.xgen.2024.100680

## SUMMARY

Illuminating the precise stepwise genetic programs directing cardiac development provides insights into the mechanisms of congenital heart disease and strategies for cardiac regenerative therapies. Here, we integrate *in vitro* and *in vivo* human single-cell multi-omic studies with high-throughput functional genomic screening to reveal dynamic, cardiac-specific gene regulatory networks (GRNs) and transcriptional regulators during human cardiomyocyte development. Interrogating developmental trajectories reconstructed from single-cell data unexpectedly reveal divergent cardiomyocyte lineages with distinct gene programs based on developmental signaling pathways. High-throughput functional genomic screens identify key transcription factors from inferred GRNs that are functionally relevant for cardiomyocyte lineages derived from each pathway. Notably, we discover a critical heat shock transcription factor 1 (HSF1)-mediated cardiometabolic GRN controlling cardiac mitochondrial/metabolic function and cell survival, also observed in fetal human cardiomyocytes. Overall, these multi-modal genomic studies enable the systematic discovery and validation of coordinated GRNs and transcriptional regulators controlling the development of distinct human cardiomyocyte populations.

## INTRODUCTION

The heart is the first organ to develop because of its critical role in circulating oxygen and nutrients throughout the body. Cardiomyocytes (CMs) are the crucial cell type that enables the heart to perform this function,[1] and their loss can lead to heart failure, a leading cause of morbidity and mortality worldwide.[2] Thus, discovering the precise molecular and genetic mechanisms of how human CMs develop, mature, and function may offer insights into a wide range of adult and congenital human cardiac diseases as well as strategies for efficiently producing new and durable CMs to treat heart failure.

Past studies have revealed that CM development is mediated through the dynamic regulation of Wnt,[3–5] bone morphogenetic protein (BMP),[6] and activin[7,8] signaling to specify the pre-cardiac mesoderm,[9–12] which produces cardiac progenitors.[13,14] Concurrently, these factors activate a series of transcription factors (TFs) including brachyury,[15,16] which then activates *EOMES*,[17] followed by *MESP1*.[18] *MESP1/2* activation is required for mesodermal migration[19–21] and subsequently induces many TFs, including *NKX2-5*,[22–24] *GATA4-6*,[25–29] *MEF2C*,[30–32] *TBX5*,[33,34] HAND1/2,[35–38] and *ISL1*,[39] as well as other regulators,[40–42] which are crucial for cardiac development. As cardiac progenitors migrate to form the cardiac crescent, they are also exposed to additional factors such as fibroblast growth factors (FGFs), which modulate the expression of the aforementioned TFs, thereby initiating myocardial differentiation.[43] Thus, the interplay between dynamic growth factor signaling and stage-specific TFs regulates the progression of heart development, which, when disrupted, can cause congenital heart disease (CHD). In particular, most CHD mutations are in transcriptional and chromatin regulators, thus highlighting the significance of a tightly regulated gene regulatory network (GRN) during cardiac development.[44–46] However, the stepwise cell-type-specific GRNs responsible for coordinating human heart development have yet to be comprehensively defined.

Single-cell sequencing technologies have facilitated the identification of gene expression programs and *cis*-regulatory landscapes in a cell-type-specific manner in human[47–52] and mouse hearts,[53–57] as well as human pluripotent stem cell (hPSC)-based

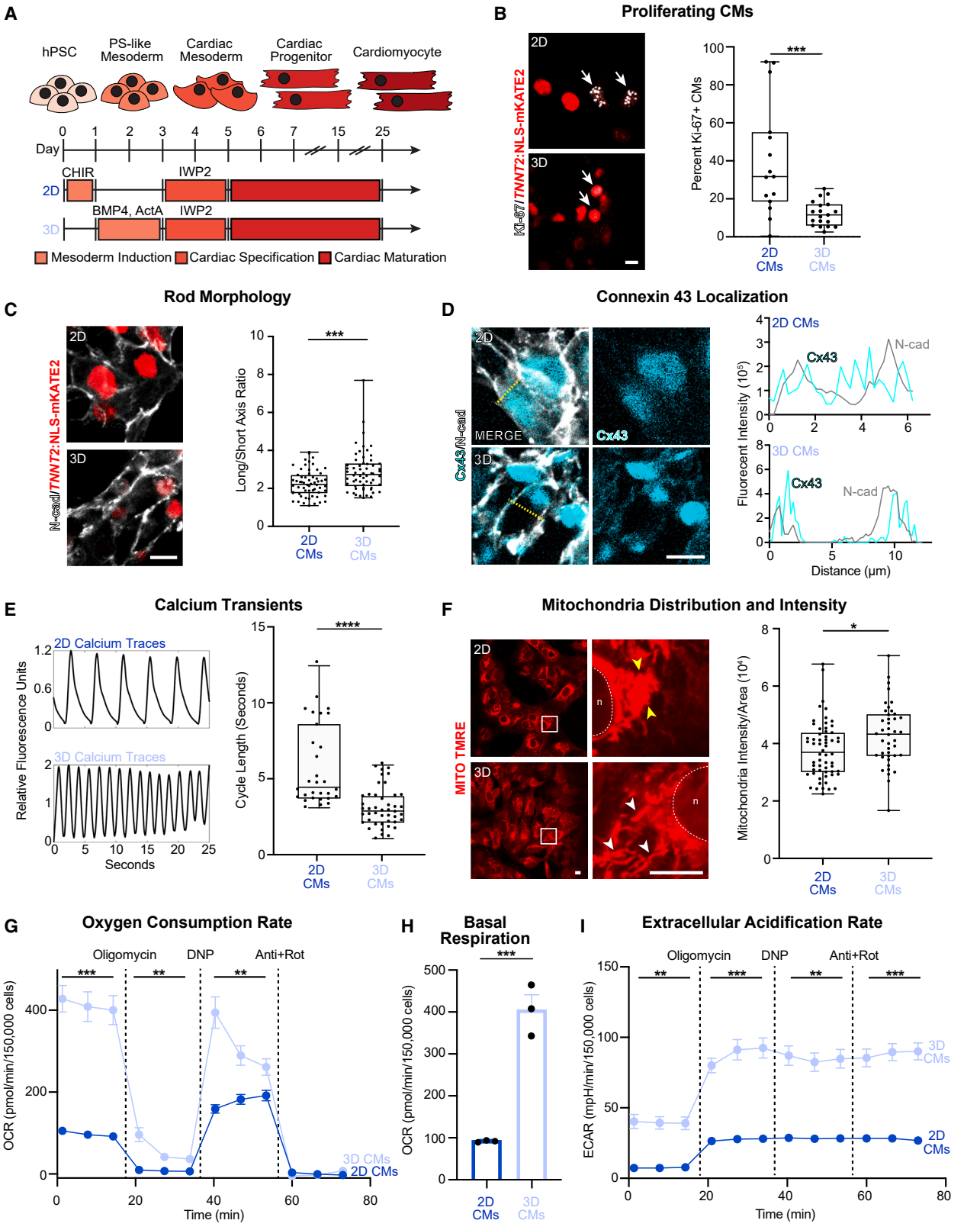


*(legend on next page)*

cardiac systems.[51,58–67] Recent computational advancements have enabled the integration of single-cell transcriptomic and *cis*-regulatory modalities, thus aiding in the reconstruction of GRNs, which direct gene programs critical for cell function,[68–71] and revealing how TFs govern dynamic cell states and transitions during development.[72] However, the GRNs that direct human cardiac development remain to be elucidated and functionally validated.

A recent technological advancement facilitating the interrogation of gene function in a high-throughput manner is CRISPR-Cas9-based screening technology. Initial genome-wide knockout (KO) screens in human cell lines illuminated the role of numerous, previously undiscovered survival genes[73,74] and thus paved the way for testing the role of genes and transcriptional regulators in more complex systems, including the heart.[75–77] As these critical studies are challenging to perform in human hearts, directed differentiation of hPSCs into CMs[78–80] *in vitro* offers the opportunity to perform screens yielding insights into human heart development and function. Specifically, CRISPR-Cas9-based screens, in conjunction with GRNs, can be used to identify and validate the impact of alterations in TF regulation and remain to be implemented on human cardiac development, particularly CMs.

Thus, to illuminate the genetic programs and key TFs that direct cardiac development, we interrogated the integrated single-cell transcriptomic and *cis*-regulatory landscapes through key stages of cardiac development using *in vitro* cardiac differentiation systems that employ different developmental signaling pathways. We investigated the dynamics of cardiac-specific GRNs and TFs that guide progenitor cells into specific stages of cardiac development. Additionally, we unveiled distinct gene regulatory programs that direct cardiac development from these *in vitro* systems, which produce functionally distinct CM populations. Employing a high-throughput functional genomic screen, we validated and prioritized crucial TFs associated with GRNs specific for each distinct developmental CM lineage, including heat shock TF 1 (HSF1), a key cardiometabolic regulator, whose gene regulation is additionally found in *in vivo* fetal human CMs. Loss of *HSF1* resulted in decreased metabolic gene expression and functional metabolic defects, which led to increased apoptosis and cellular impairment, thus illustrating the importance of HSF1 as a regulator during CM development. Together, these findings define the transcriptomic and chromatin landscape of early cardiac development, infer the GRNs that govern cardiac development and function, validate the TFs predicted to control these GRNs, and reveal HSF1 as an essential cardiometabolic regulator during the development of early human CMs.

## RESULTS

### CMs derived from Wnt-based 2D- and BMP/ActA-based 3D-hPSC cardiac differentiation systems exhibit functional differences

hPSC cardiac systems have been developed as models to understand human heart development, utilizing signaling pathways such as Wnt, BMP, and Activin A (ActA).[59,61,64,80–82] By using established protocols for hPSC differentiation into CMs via Wnt-based two-dimensional (2D)-[81] and BMP/ActA-based 3D-hPSC[80] systems (Figure 1A), we generated high yields of functional CMs as detected using fluorescent reporter lines for *TNNT2*[83] (Figures S1A–S1C). Functional analysis revealed that 2D hPSC-CMs exhibited significantly higher levels of proliferation as compared to 3D hPSC-CMs (Figure 1B), suggesting that 3D hPSC-CMs may be more mature, as CMs lose their capacity to proliferate postnatally.[84] Additionally, 3D hPSC-CMs displayed a more rod-shaped morphology as compared to the 2D hPSC-CMs (Figure 1C), supporting the matured structural morphology[85] in 3D hPSC-CMs. 3D hPSC-CMs also presented peripheral localization of Connexin 43 (Cx43), as identified by co-localization with neural cadherin (N-cad), whereas the 2D hPSC-CMs did not (Figure 1D), suggesting improved cellular coupling of 3D hPSC-CMs allowing for the propagation of electrical signals between cells.[86] Finally, 3D hPSC-CMs exhibited faster calcium transients (19.0 ± 10.0 transients/min), which were closer to a physiological rate, than 2D hPSC-CMs (10.2 ± 4.4 transients/min) (Figure 1E).

Because metabolic maturation is crucial for heart development *in vivo*,[87,88] we analyzed the metabolic features of these hPSC-CMs. We observed perinuclear localization of aggregated mitochondria in the 2D hPSC-CMs, whereas mitochondria in the 3D hPSC-CMs were more uniformly distributed and at a higher density as compared to 2D-derived CMs (Figure 1F). As mitochondria localization and distribution impact metabolic function,[89,90] we measured the metabolic capacity of the 2D and

**Figure 1. Wnt-based 2D monolayer- and BMP/Activin A-based 3D embryoid body-derived hPSC-CMs display distinct functional differences**

(A) Schematic of 2D and 3D hPSC-CM differentiation systems.

(B) Immunostaining (left) and quantification (right) of proliferating CMs (Ki-67+ and *TNNT2*+, as represented by arrows) ($n$ = 15–18).

(C) Immunostaining (left) and quantification (right) reveal rod-shaped morphology using N-cad as a marker for cell boundary ($n$ = 3, 20 hPSC-CMs/condition).

(D) Immunostaining of N-cad for cell boundary and Cx43 for gap junctions (left) and quantification of antibody fluorescent intensity (right) based on dashed yellow line.

(E) Spontaneous calcium transient traces (left) and boxplot showing cycle length (right) ($n$ = 3, 6–16 hPSC-CMs/condition).

(F) Immunostaining (left) and quantification (right) reveal mitochondria distribution and intensity ($n$ = 3; 15 hPSC-CMs/condition). Inset shows high-magnification views of the regions outlined by white box. Yellow arrowheads point to regions of aggregated mitochondria, whereas white arrowheads point to regions of well-distributed mitochondria. Dashed line: nucleus (n).

(G) Oxygen consumption rate (OCR) analysis ($n$ = 3; $n$ = 4–6 technical replicates/condition).

(H) Basal respiration rate ($n$ = 3; $n$ = 4–6 technical replicates/condition).

(I) Extracellular acidification rate (ECAR) analysis ($n$ = 3; $n$ = 4–6 technical replicates/condition).

(B, C, and E–I) Data were analyzed using a two-tailed Student's t test. $p < 0.05$, $^{*}p < 0.05$, $^{**}p < 0.01$, $^{***}p < 0.001$, and $^{****}p < 0.0001$. Data are represented as mean ± SEM. Scale bar: 10 μM. pmol, picomole; min, minutes; Anti+Rot, Antimycin A and rotenone; mpH, 1/1,000th pH unit.

See also Figure S1.

3D hPSC-CMs (Figures 1G–1I). We found that 3D hPSC-CMs display significantly increased basal respiration, maximal respiration, and extracellular acidification rates as compared to 2D hPSC-CMs, thereby supporting that 3D hPSC-CMs are more metabolically active than 2D hPSC-CMs (Figures 1G–1I). Consistent with previous findings,[91–93] we found that 3D hPSC-CMs may be structurally, functionally, and metabolically more mature than 2D hPSC-CMs.

## Single-cell multi-omic studies reveal distinct developmental stages of fate decisions during CM development

To investigate the molecular mechanisms driving hPSC differentiation into functionally distinct CMs, we interrogated the gene expression and chromatin landscape of cell populations generated from these protocols. We collected cells at six stages throughout cardiac differentiation as we described[94,95] for single-cell RNA sequencing (scRNA-seq) and single-nucleus assay for transposase-accessible chromatin with sequencing (snATAC-seq) (Figure 2A; Table S1). Using Seurat[96] and ArchR,[97] we identified 31 scRNA-seq clusters and 23 snATAC-seq clusters, which were annotated using known cell-type-specific marker genes to arrive at 12 distinct cell populations (Figures S2A–S2D; Table S1). These cell populations included hPSC, primitive streak (PS), mesendoderm, pre-somitic mesoderm (PSM), lateral plate mesoderm (LPM), cardiac mesoderm, CM, endoderm, vascular endothelial (VE), mesenchymal progenitor (MP), epithelium, and neuromesodermal progenitor (NMP) populations (Figures 2B and S2A–S2D). To validate our cell population annotations, we performed cell label transfers on our identified cell populations using previously published *in vivo* developmental datasets[98,99] and found a high correlation for many of the cell population labels between the *in vitro* and *in vivo* single-cell datasets (Figure S2E). After defining these cell populations, the two sequencing modalities were integrated onto each other, revealing the high correlation between the cell populations within the integrated datasets with minimal cell population loss; however, the epithelium population was absent from the snATAC-seq dataset, presumably due to low cell numbers combined with the limited dynamic range and specificity of snATAC-seq as compared to scRNA-seq[100–102] (Figures S2F and S2G). Further investigation of these cell populations revealed that 2D-differentiated hPSCs initially formed mesendoderm, whereas 3D-differentiated hPSCs created PS and then LPM, supporting differences in the growth factors used for producing CMs between the differentiation systems[5] (Wnt versus BMP/ActA based, respectively; Figures S2C and S2D). Thus, these early developmental differences between the cardiac differentiation systems likely lead to distinct cardiac mesoderm and CM populations (Figures S2C and S2D).

To understand how these differences emerge during CM generation from hPSCs between 2D and 3D cardiac differentiation systems, we organized cells from our integrated single-cell multi-omic dataset along developmental trajectories using the lineage inference tool URD.[103] These reconstructed paths ordered cells along a pseudotime axis, aligning with the differentiation time points, and unveiled branchpoint decisions governing the different cell populations in 2D and 3D systems (Figures 2C and S3). In particular, we observed early branching of endoderm from mesendoderm and, subsequently, LPM from PSM, the former becoming the CM lineage and the latter becoming the MP and VE populations (Figure 2C). Further examination of the CM lineage developmental trajectory enabled the interrogation of the gene expression and motif enrichment dynamics, including the genetic program differences at the developmental branchpoint between 2D and 3D hPSC-CMs (Figures 2C and 2D). Specifically, we discovered that 2D hPSC-CMs maintained chromatin accessibility in early stem/progenitor genes (e.g., *SOX2*) but were unable to activate the genetic programs of important cardiac marker genes (e.g., *NKX2-5*) (Figure 2E). Moreover, these early gene program differences may impact downstream gene expression and chromatin accessibility, resulting in distinct gene programs and transcriptional regulators (Table S2). For instance, 2D hPSC-CMs primarily express broad cell differentiation gene programs (e.g., *MYH7*, *COL2A1*, *ANKRD1*) and utilize TEA domain (TEAD) and AP-1 (e.g., JUND, FOSL2) TFs, whereas 3D hPSC-CMs specifically express metabolic gene programs (e.g., *DES*, *CKM*, *MB*) and utilize MEF and NFI TF family members (Figures 2D and 2E; Table S2). Thus, the divergent developmental trajectories of 2D and 3D hPSC-CMs may explain their functional differences.

## Reconstructed GRNs of cardiac lineages reveal the stepwise coordinated genetic programs controlling human CM development

To identify the gene regulatory programs controlling CM development from 2D- and 3D-hPSC cardiac differentiation systems, we constructed GRNs by integrating our single-cell transcriptomic and chromatin accessibility data using the GRN inference package Pando[68] (Figure 3A; Table S2). These inferred GRNs were subsequently visualized using a uniform manifold approximation and projection (UMAP) embedding, identifying hundreds of TFs that regulate the developmental stage transitions from mesendoderm (e.g., EOMES, ZIC3) and LPM (e.g., ISL1, NR2F1), into cardiac mesoderm (e.g., HAND2, GATA4), and finally into 2D and 3D hPSC-CMs (e.g., MEF2C, TBX5) (Figure 3B; Table S2). Applying pseudotime derived from our trajectory analyses onto these GRNs revealed the progressive activation of TFs and GRNs during CM development (Figure 3B). In particular, we identified known TF regulators and regulatory interactions both early and late in CM development (e.g., HAND2 activates *GATA4*,[104] NKX2-5[105] and ISL1[106] activate *MEF2C*, and TBX5 activates *NKX2-5*[107]). Many of these TFs display high degree centrality scores (Figures 3B and S4A; Table S2), reflecting the interconnectedness of these TFs with the inferred cardiac GRN. We also uncovered unexpected TF regulation including the inhibition of *GATA4* by mesendoderm TFs ZIC2 and ZIC3 and the activation of *GATA4* by LPM TFs NR2F1 and HAND1, which may underlie some of the developmental differences between 2D and 3D hPSC-CMs (Figure 3B; Table S2). Globally, this CM lineage GRN reveals that the chromatin accessibility of regulatory regions and the expression of TFs align with distinct stages of cardiac development.

To understand the differences in GRN activity within CMs between the two cardiac differentiation systems, we analyzed the

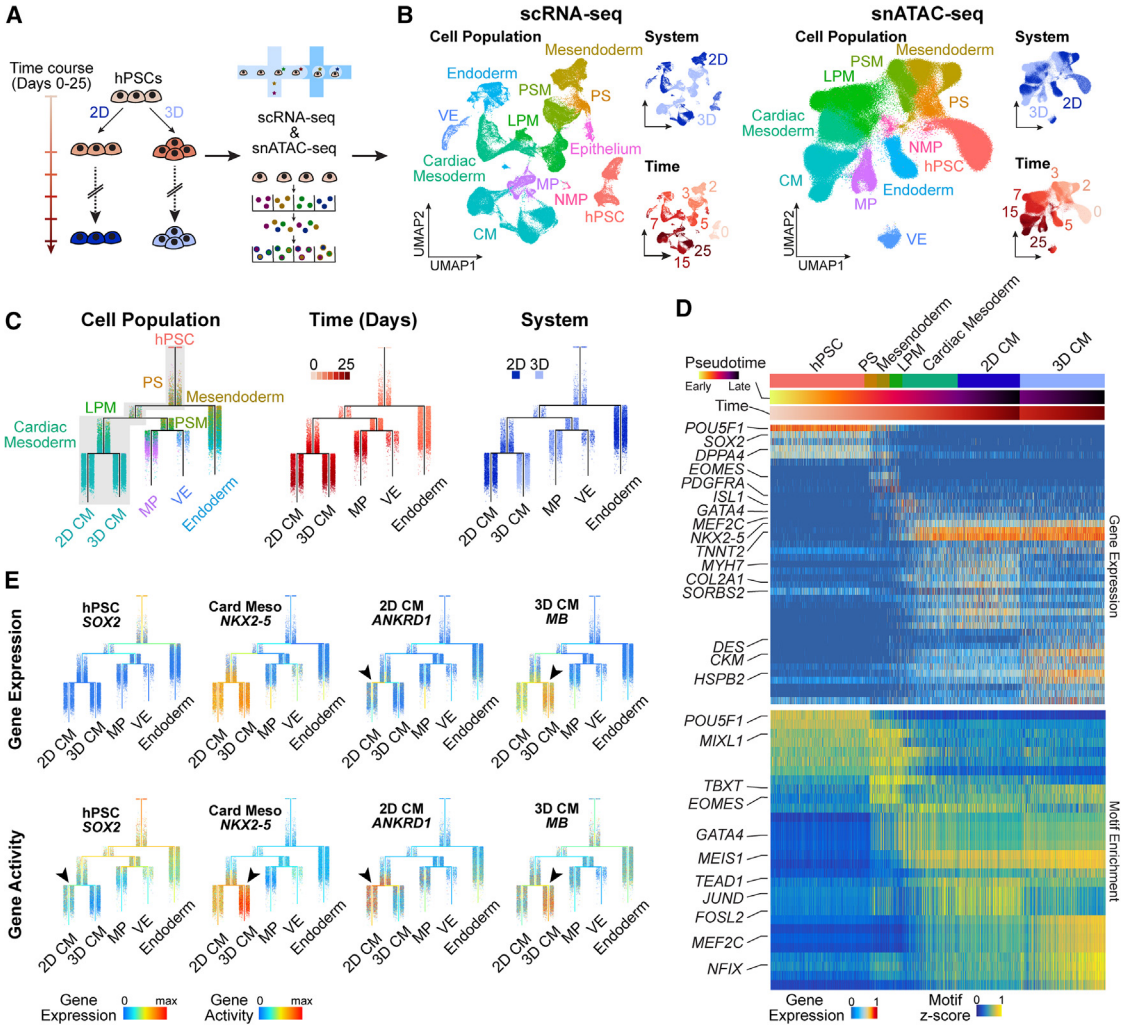


**Figure 2. Single-cell multi-omic studies and trajectory analysis uncover specific developmental CM lineages and their respective gene regulatory programs**

(A) Schematic of scRNA-seq and snATAC-seq workflows of 2D and 3D hPSC-CM differentiations over six developmental stages.

(B) scRNA-seq (left) and snATAC-seq (right) UMAP visualization represented by cell population, differentiation system (top right), and time in days (bottom right) for 2D and 3D hPSC-CM differentiations.

(C) Developmental trajectory of differentiation systems displayed by cell population (left), time (middle), and differentiation system (right). Developmental trajectory of CM lineage is shaded in gray from hPSCs to distinct 2D and 3D hPSC-CMs utilized in (D).

(D) Heatmap of developmental CM lineage trajectory displays dynamic gene expression and motif enrichment *Z* score throughout pseudotime and collection time point.

(E) Gene expression (top) and gene activity based on chromatin accessibility (bottom) for representative marker genes for specific cell populations are mapped on to developmental trajectories. Arrowheads point to major differences in gene expression and chromatin accessibility between differentiation systems.

max, maximum.

See also Figures S2 and S3.

GRNs that regulate the 2D and 3D hPSC-CM URD trajectory branches to identify cardiac-system-specific gene regulation (Figure 3C; Table S2). We partitioned the overall CM lineage GRN into a trajectory branch-specific GRN, built from differential TFs at the trajectory branchpoint (Figures 3C and S4B; Table S2). This branch-specific GRN revealed shared TFs such as those in the Meis homeobox (MEIS) and Pbx homeobox (PBX) TF families as well as system-specific TFs for 2D (e.g., FOS, JUN, T cell factor [TCF], and TEAD TF families) and 3D hPSC-CMs (e.g., HSF TF family, MEF2C) (Figure 3C; Table S2). Notably, TCF4 and TCF7L2, pre-branchpoint TFs, were predicted to regulate *TEAD1* and *JUN*, respectively, which control post-branchpoint GRNs specific to the 2D hPSC-CM differentiation system, demonstrating the temporal dynamics of these cardiac GRNs (Table S2). Globally, 2D hPSC-CM lineage GRNs were enriched for genes associated with muscle development and system development processes, exemplified by *TOP2A*, *TTN*, and *TUBA1A* gene regulation, whereas 3D hPSC-CM lineage GRNs

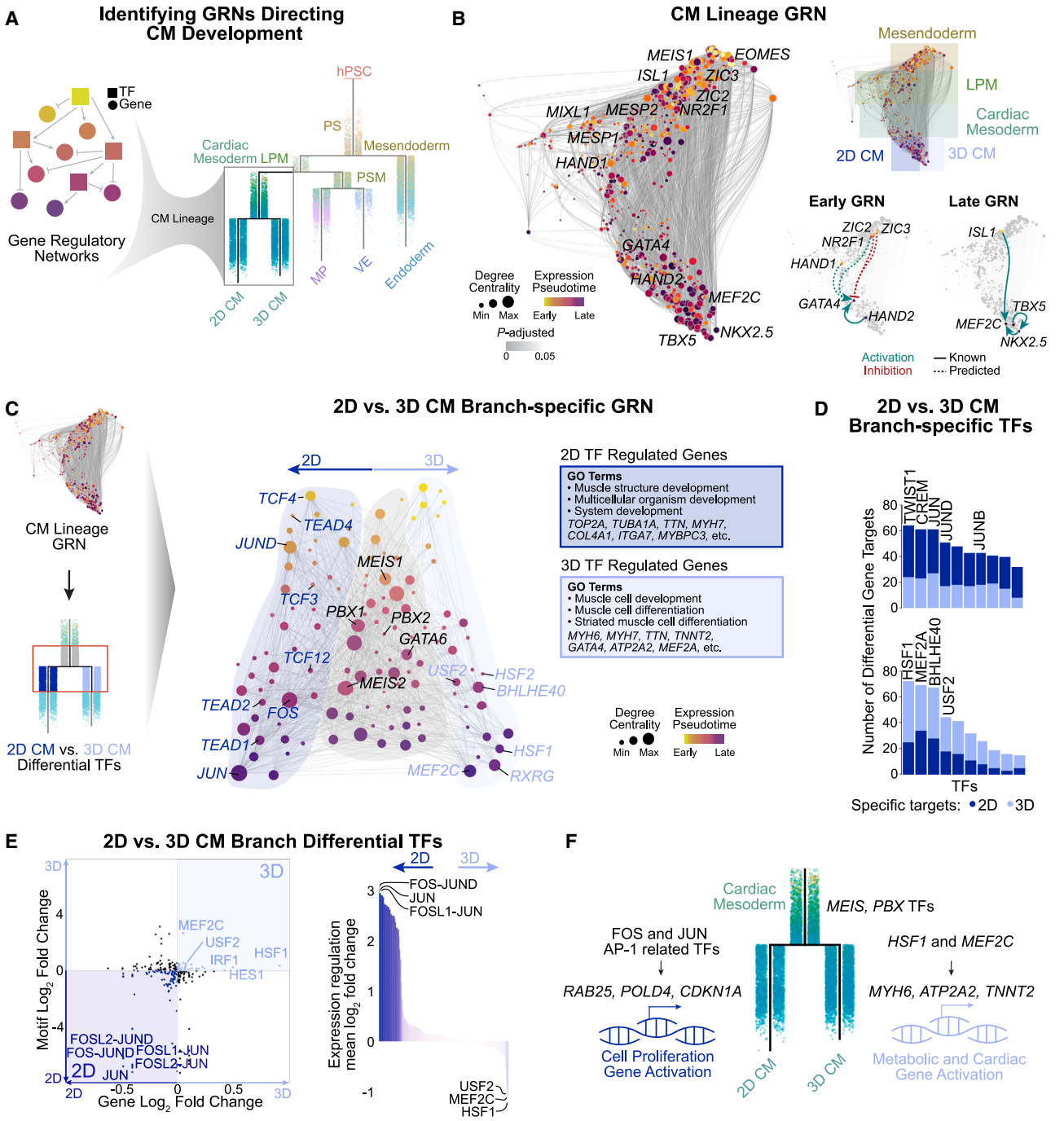


**Figure 3. Interrogating joint transcriptional profiles and chromatin accessibility uncovers distinct gene regulatory programs during cardiac development**

(A) Schematic of how GRNs are generated using Pando for the CM lineage.

(B) UMAP embedding of the inferred CM lineage TF network based on correlation between TFs. Node size represents degree centrality, node color represents expression-weighted pseudotime, and edge color represents adjusted *p* value of the inferred interactions. UMAP embedding in the top right is shaded by cell population. UMAP embeddings in the bottom right highlight examples of previously known (solid line) and predicted (dashed line) TF interactions, with green lines representing activated and red lines representing inhibited gene regulation.

(C) Interrogating CM lineage TF network specifically at the branchpoint of CM lineage developmental trajectory reveals the distinct TFs in 2D and 3D hPSC-CMs. Schematic shows how 2D versus 3D CM branch-specific GRNs were generated by integrating CM lineage GRNs with differentially expressed TFs at the branchpoint of the CM lineage developmental trajectory (left). Gene Ontology (GO) terms for genes regulated by the 2D- or 3D-hPSC system-specific TFs (right).

(D) Bar plot shows differential gene target specificity for 2D- (top) and 3D-hPSC (bottom) system-specific TFs.

*(legend continued on next page)*

were enriched for genes associated with muscle differentiation processes, including *MYH6*, *TNNT2*, and *ATP2A2* gene regulation (Figure 3C; Table S2).

To identify cardiac-system-specific TF regulation, we classified TFs by their branch-specific gene target sets, defined by genes enriched in 2D or 3D hPSC-CMs (Figure 3D; Table S2). TFs such as TWIST1, CREM, and AP-1-related TFs (e.g., JUN, JUND, and JUNB) regulated more 2D-hPSC system-specific target genes, while HSF1, MEF2A, and BHLHE40 regulated more 3D-hPSC system-specific target genes (Figure 3D). To prioritize the TFs likely contributing to the regulation of the bifurcation between 2D and 3D hPSC-CMs, we identified branch-specific active TFs based on the differential gene expression and motif utilization at the branchpoint. We discovered that AP-1-related TFs, which are involved in cell proliferation, are the most active in the 2D-hPSC system, whereas MEF2C and HSF1, which are involved in heart development and metabolic processes, are the most active in the 3D-hPSC system (Figure 3E; Table S2). This finding aligns with the high degree centrality of these TFs, supporting their activity and interconnectedness within each cardiac-system-specific GRN (Figure S4B). Through these analyses, we identified early shared TFs (e.g., MEIS- and PBX-related TFs) within developing CMs as well as differentially expressed TFs between the CM differentiation systems, which allow for CM system-specific gene regulation (e.g., AP-1-related TFs activating cell proliferation genes in the 2D-hPSC system, MEF2C and HSF1 activating metabolic and cardiac genes in the 3D-hPSC system) (Figure 3F). Thus, these gene regulatory programs provide insights into the dynamic GRNs throughout CM development and system-specific GRNs differentiating 2D and 3D hPSC-CMs, potentially explaining the functional differences identified between systems.

## CRISPR-Cas9 KO screen uncovers TFs important in CM development

To complement our inferred GRN analyses and functionally interrogate how TFs impact CM differentiation between *in vitro* systems, we employed a comprehensive CRISPR-Cas9 TF KO screen for 1,639 TFs (Figures 4A and S4C–S4G; Table S3).[108] By analyzing the single guide RNA (sgRNA) enrichment in the CM and non-CM cell populations ($n$ = 3 biological replicates/condition), we identified TFs promoting or blocking CM differentiation as evidenced by enrichment of sgRNAs in non-CMs or CMs, respectively. The 2D-hPSC TF KO screen identified 155 TFs promoting and 98 TFs blocking CM differentiation, whereas the 3D-hPSC TF KO screen identified 112 TFs promoting and 411 TFs blocking CM differentiation (Figures 4B and 4C; Table S3). Although there were more TFs differing between CM differentiation methods, there were 13 overlapping TFs promoting and 21 overlapping TFs blocking CM differentiation between 2D- and 3D-hPSC systems (Figure S4H). These factors contained known TFs including THRA, a heart development regulator,[109] which promoted CM differentiation in both systems, and, by contrast, NANOG, a pluripotency regulator,[110] which blocked CM differentiation in both systems (Figure S4H). Moreover, while many of the TFs blocking CM differentiation were different between systems, the majority were involved in developing non-cardiac lineages, including those of non-cardiogenic mesoderm origin, such as SOX8 in kidney development[111] and OLIG3 in spinal cord development[112] in 2D- and 3D-hPSC systems, respectively, thus suggesting that inhibiting other germ layers may promote CM lineage development in both systems (Figures 4B and 4C).

To investigate TF-driven gene regulation differences between the *in vitro* CM differentiation systems, we analyzed the TFs that promoted CM differentiation in each system. In the 2D-hPSC system, early developmental TFs, in particular those in the β-catenin pathway (e.g., TCF4, TCF7L2, etc.) that can specify early mesoderm,[113] were identified (Figure 4B; Table S3). Conversely, the 3D-hPSC system contained many known cardiac TFs involved in reprogramming (e.g., NKX2-5, GATA4, etc.) (Figure 4C; Table S3). Thus, TFs promoting CM differentiation in the 2D-hPSC system were primarily involved in early mesendoderm development, whereas those in the 3D-hPSC system were late cardiac TFs, aligning with the GRN findings (Figures 3B, 3C, 4B, and 4C). Ultimately, our CRISPR-Cas9 TF KO screen identified both known and unknown TFs that regulate CM differentiation in 2D- and 3D-hPSC systems, providing valuable insights for optimizing directed CM differentiation.

To uncover how these TFs function in each cardiac-system-specific GRN, we constructed individual GRNs for 2D and 3D hPSC-CM lineages inferred from Pando and analyzed the role of these genomic screen candidates in each GRN (Figures 4D, S4I, and S4J; Table S3). This analysis identified 5 shared and 72 and 52 functionally significant TFs in the 2D and 3D hPSC-CM lineages, respectively (Figure 4D; Table S3). Furthermore, TFs in the top 10% of our 2D CM GRN were 1.8 times more enriched in the screen than those in the bottom 10%, based on degree centrality (Table S3). In the 3D CM GRN, the top 10% of TFs displayed 2.7 times greater enrichment in the screen than the bottom 10% (Table S3). In both systems, known cardiac TFs including THRA[109] and IRX3[114,115] were identified, revealing shared regulatory mechanisms within *in vitro* CM development (Figure 4D). Conversely, TCF-related TFs functioning in the β-catenin pathway and cardiac developmental TFs were validated in 2D- and 3D-hPSC systems, respectively (Figure 4D), revealing the essential TFs for directed CM differentiation in each system.

To investigate whether these TFs regulate differences between 2D and 3D hPSC-CMs, we filtered the functionally validated TFs to retain those active at the CM trajectory branchpoint, identifying seven TFs in the 2D-hPSC system and two TFs in the 3D-hPSC system (Figures 4E, S4K, and S4L). We identified known regulators including three TCF-related TFs in the

(E) Scatterplot reveals TFs active in 2D and 3D hPSC-CMs based on differentially expressed genes versus differential motif utilization (left). Bar plot shows integrative TF ranking between 2D and 3D hPSC-CMs using the mean $\log_2$(fold change) of differential expression and motif utilization (right).
(F) Schematic of the identified gene regulatory differences before and after the CM branchpoint between *in vitro* cardiac systems.
min, minimum.
See also Figure S4.

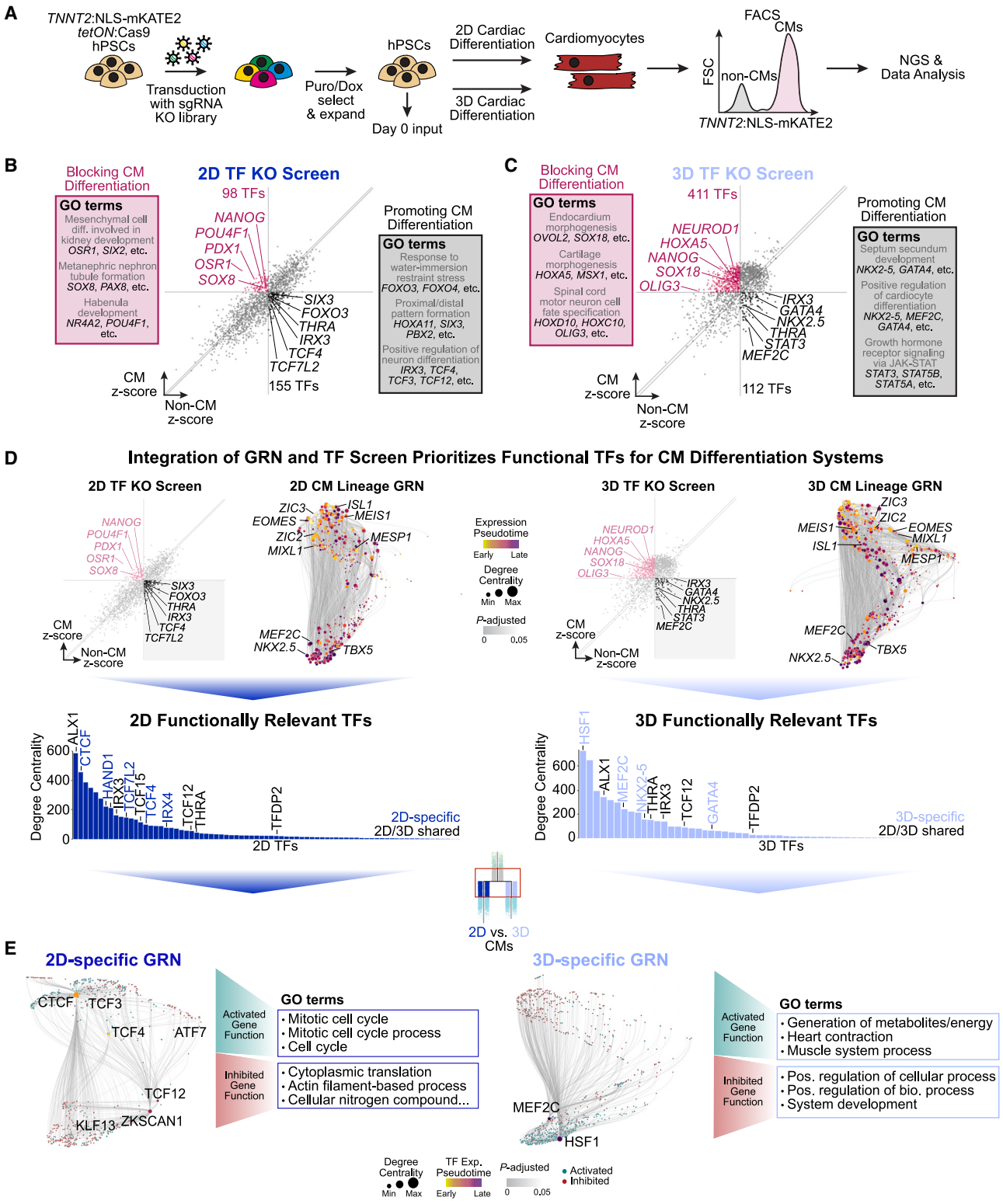


**Figure 4. CRISPR-Cas9 KO screen reveals functionally relevant transcriptional regulators during CM development**

(A) Schematic of the CRISPR-Cas9 KO screening strategy.

(B and C) Scatterplots display TFs (representing the average of seven guides analyzed in three biological replicates) that promote (black) or block (dark pink) CM differentiation in (B) 2D- and (C) 3D-hPSC systems based on TF *Z* score enrichment. The top three GO terms associated with these TFs are shown.

*(legend continued on next page)*

2D-hPSC system, involved in mesendoderm formation,[116,117] and MEF2C in the 3D-hPSC system, some of which are involved in cardiac development.[118,119] Additionally, we discovered previously unknown CM regulators including ATF7, CTCF, KLF13, and ZKSCAN1 in the 2D-hPSC system and HSF1 in the 3D-hPSC system (Figure 4E). To understand the role of these TFs in cardiac development, we analyzed their GRNs to reveal the interconnectedness among co-regulated genes by the identified TFs (Figure 4E). 2D-hPSC system-specific TFs co-regulated genes involved in cell cycle processes, including *AURKB*, *CCNA2*, and *CDC25B* genes, whereas 3D-hPSC system-specific TFs co-regulated genes involved in metabolism and heart contractility processes, including *ACADVL* and *NDUFS2* and *MYH7* and *TNNT2* genes, respectively (Figures 4E and S4M; Table S3). The finding that 2D hPSC-CMs expressed cell cycle regulators was consistent with the increased levels of Ki-67, a marker of proliferation, in 2D hPSC-CMs versus 3D hPSC-CMs (Figure 1B). By integrating our screen candidates with the cardiac-system-specific GRNs and branchpoint-specific TFs from the URD trajectory, we uncovered how cardiac-system-specific TFs and their gene regulatory programs may regulate CM development between different differentiation systems.

## HSF1 directly regulates cardiometabolic function

HSF1, a top regulator of CM differentiation enriched in 3D hPSC-CMs (Figures S5A and S5B), was also identified through a 3D-hPSC system-specific CRISPR-Cas9 KO screen (Figure 4). Consistent with its role in regulating cellular homeostasis and metabolism by modulating the oxidative state of the mitochondria,[120–124] our 3D CM lineage GRNs show that HSF1 activates mitochondria- and metabolic-related genes including *COX6A2*, *MTFR1L*, and *ATP5F1A* (Table S4). However, how HSF1 may regulate cardiac development remains unclear.

To investigate the role of HSF1, we generated three clonal *HSF1* KO hPSC lines, differentiated them into 3D hPSC-CMs, and performed transcriptomic analyses (Figures 5A, 5B, and S5C–S5E; Table S4). *HSF1* KO hPSC-CMs displayed upregulated genes within the Gene Ontology (GO) category of system development (e.g., known developmental genes SOX2[125] and LIN28A[126]) (Figure 5B; Table S4). Conversely, control hPSC-CMs exhibited upregulated genes in metabolic processes (e.g., known metabolic genes *CAT*[127] and *HMGCS2*[128]) (Figure 5B; Table S4). We also observed significant overlap between the differentially expressed genes in *HSF1* KO hPSC-CMs and the predicted genes regulated by HSF1 from the 3D hPSC-CM lineage GRN, including many involved in metabolic processes such as *PLCB2*, *DECR1*, and *AK4* (Figure 5C).

We examined how *HSF1* loss of function may lead to metabolic changes within CMs. As HSF1 is a known modulator of oxidative stress, we observed increased reactive oxygen species (ROS; normalized to mitochondria content) in *HSF1* KO hPSC-CMs, suggesting that HSF1 regulates oxidative stress in CMs (Figure 5D). Contrasting the widespread, uniform distribution of mitochondria within the control hPSC-CMs, we observed perinuclear aggregation of mitochondria coinciding with ROS localization in *HSF1* KO hPSC-CMs, which has been reported in other cell systems[129] (Figure 5D). However, there was no significant difference in mitochondria quantity between the *HSF1* KO and control hPSC-CMs (Figure S5F), indicating that HSF1 impacts mitochondria localization rather than quantity (Figure 5D). As mitochondria localization is important for CM function,[89,90] we measured metabolic capacity using the Seahorse mitochondria stress test (Figures 5E, 5F, and S5G–S5K). *HSF1* KO hPSC-CMs were less energetic and more quiescent as exemplified by significantly reduced basal respiratory capacity, mitochondria coupling, non-mitochondria oxygen consumption, and ATP production compared to control hPSC-CMs (Figures 5E, 5F, and S5G–S5K). These metabolic alterations are indicative of decreased mitochondrial function and a quiescent metabolic state in the *HSF1* KO hPSC-CMs (Figures 5E, 5F, and S5G–S5K). Therefore, loss of *HSF1* within CMs leads to defects in mitochondria localization and metabolic function.

Because *HSF1* is an essential candidate regulator of CM differentiation identified from our CRISPR-Cas9 TF KO screen (Figure 4E), we also investigated whether the HSF1-dependent defects in mitochondria localization and metabolic function may lead to reduced numbers of CMs and/or increased cell death. CM percentage was significantly reduced in the *HSF1* KO as compared to control (Figure S5L). To examine whether the decrease in CMs in the *HSF1* KO was a function of increased cell death in CMs, we analyzed the percentage of apoptotic cells and found a 2-fold increase in cell death in the *HSF1* KO hPSC-CMs versus control (Figure 5G). Altogether, these findings reveal that HSF1 is important in maintaining metabolic homeostasis through its regulation of metabolic and mitochondrial genes in CMs, which, when impaired, results in functional defects including increased ROS, reductions in mitochondrial distribution, and decreased ATP production, therefore leading to increased CM cell death (Figure 5H).

## HSF1 is a potential regulator in the developing human heart

To investigate whether HSF1 may be a key regulator in CMs within the early human heart, we integrated scRNA-seq[96] and snATAC-seq[97] of a developing human heart at 15 post-conception weeks (PCW) to construct a CM-based GRN and analyze the regulatory role of HSF1 (Figures 6A and S6A–S6F; Table S5). The CM-specific GRN generated from the 15 PCW fetal heart data revealed many

(D) Schematic shows strategy for prioritizing functional TFs by integrating screen candidates and system-specific GRNs (2D-hPSC system, top left, and 3D-hPSC system, top right). Bar plot shows the ranking of functionally validated TFs by degree centrality in the 2D- (bottom left) and 3D-hPSC systems (bottom right). System-specific TFs are highlighted in blue, and shared TFs between systems are highlighted in black.
(E) UMAP embedding displays the functionally validated TFs in the 2D (left) and 3D system-specific hPSC-CM GRNs (right). Gene node color represents an activated or inhibited gene. GO terms are presented for the activated (green) and inhibited (red) genes for each differentiation method.
dox, doxycycline; FACS, fluorescence-activated cell sorting; FSC, forward scatter; NGS, next-generation sequencing; diff, differentiation; exp, expression; pos, positive.
See also Figure S4.

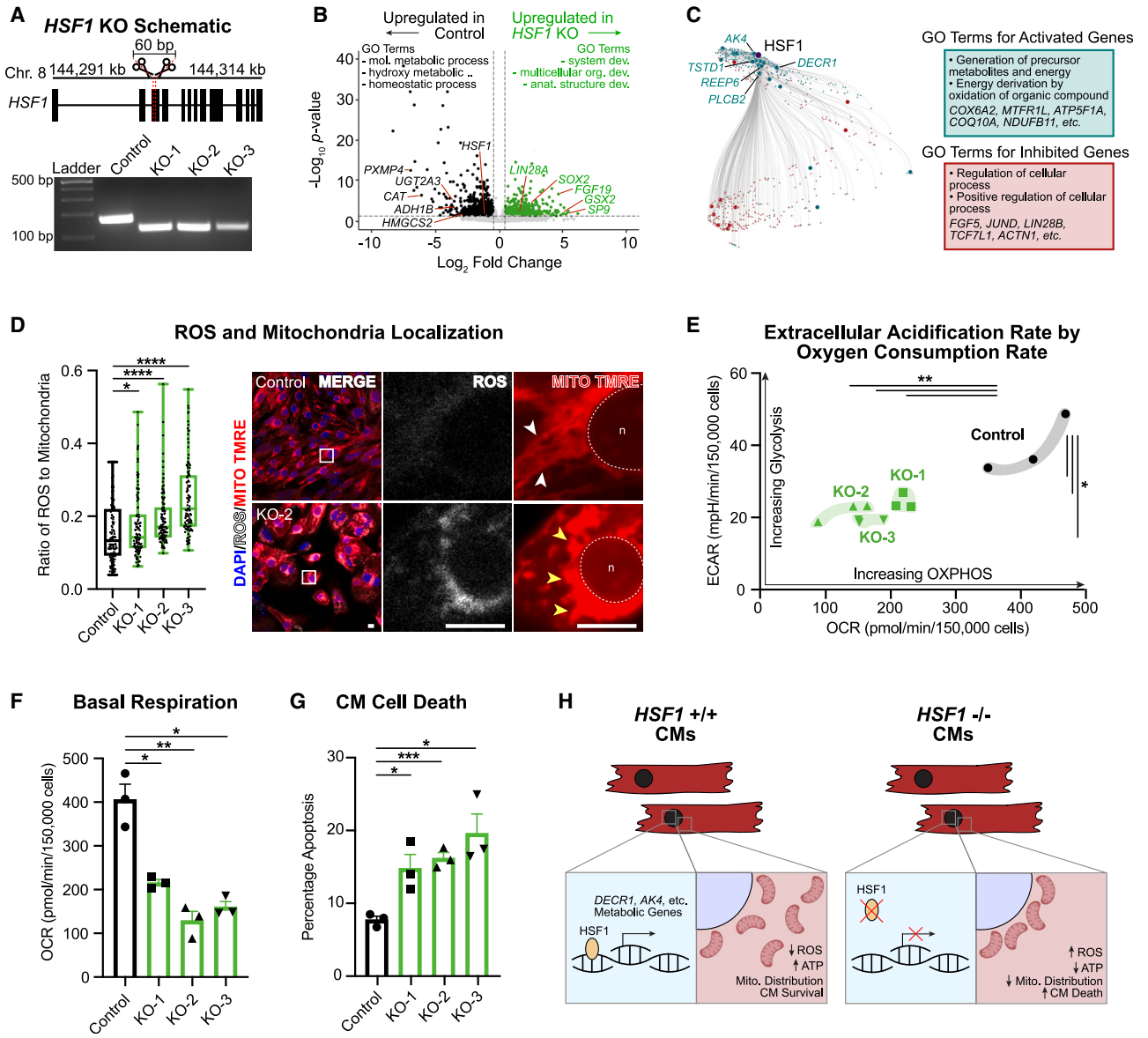


**Figure 5. Loss of HSF1 function results in dysregulation of metabolic genes, improper mitochondria localization, and reduced metabolic function**

(A) Targeting strategy to generate hPSC *HSF1* KO lines (top). PCR genotyping confirmed three hPSC *HSF1* KO lines (versus the control hPSC line), cropped to remove the righthand ladder (bottom).

(B) Volcano plot shows top differentially expressed genes (dashed lines demarcate $\log_2$(fold change) > 0.5 and adjusted $p < 0.05$) between control and *HSF1* KO hPSC-CMs with GO terms for differentially expressed genes.

(C) UMAP embedding of the 3D CM lineage GRN specific for *HSF1* reveals genes activated (green) and inhibited (red) by *HSF1* including top GO terms with some of their associated genes. Enlarged nodes represent genes identified in both the 3D CM lineage GRN and differential bulk RNA-seq data between *HSF1* KO and control hPSC-CMs.

(D) Quantification (left) and immunostaining (right) display ROS and mitochondria localization and intensity ($n$ = 3; 45 hPSC-CMs/condition). Insets are high-magnification views of the regions outlined by white box (right) with white arrowheads pointing to regions of well-distributed mitochondria and yellow arrowheads pointing to regions of aggregated mitochondria. Scale bar: 10 μM. Dashed line: nucleus (n).

(E) Scatterplot of extracellular acidification rate (ECAR) versus oxygen consumption rate (OCR) ($n$ = 3; $n$ = 6 technical replicates/condition).

(F) Basal respiration rate ($n$ = 3; $n$ = 6 technical replicates/condition).

(G) Bar plot shows CM cell death ($n$ = 3; 200 hPSC-CMs/condition).

(H) Schematic illustrates how *HSF1* functions in hPSC-CMs.

(D–G) Data were analyzed using a two-tailed Student's t test. $p < 0.05$, *$p < 0.05$, **$p < 0.01$, ***$p < 0.001$, and ****$p < 0.0001$. Data are represented as mean ± SEM. bp, base pair; kb, kilobase; chr, chromosome; mol, molecule; dev, development; ns, not significant; mito, mitochondria.

See also Figure S5.

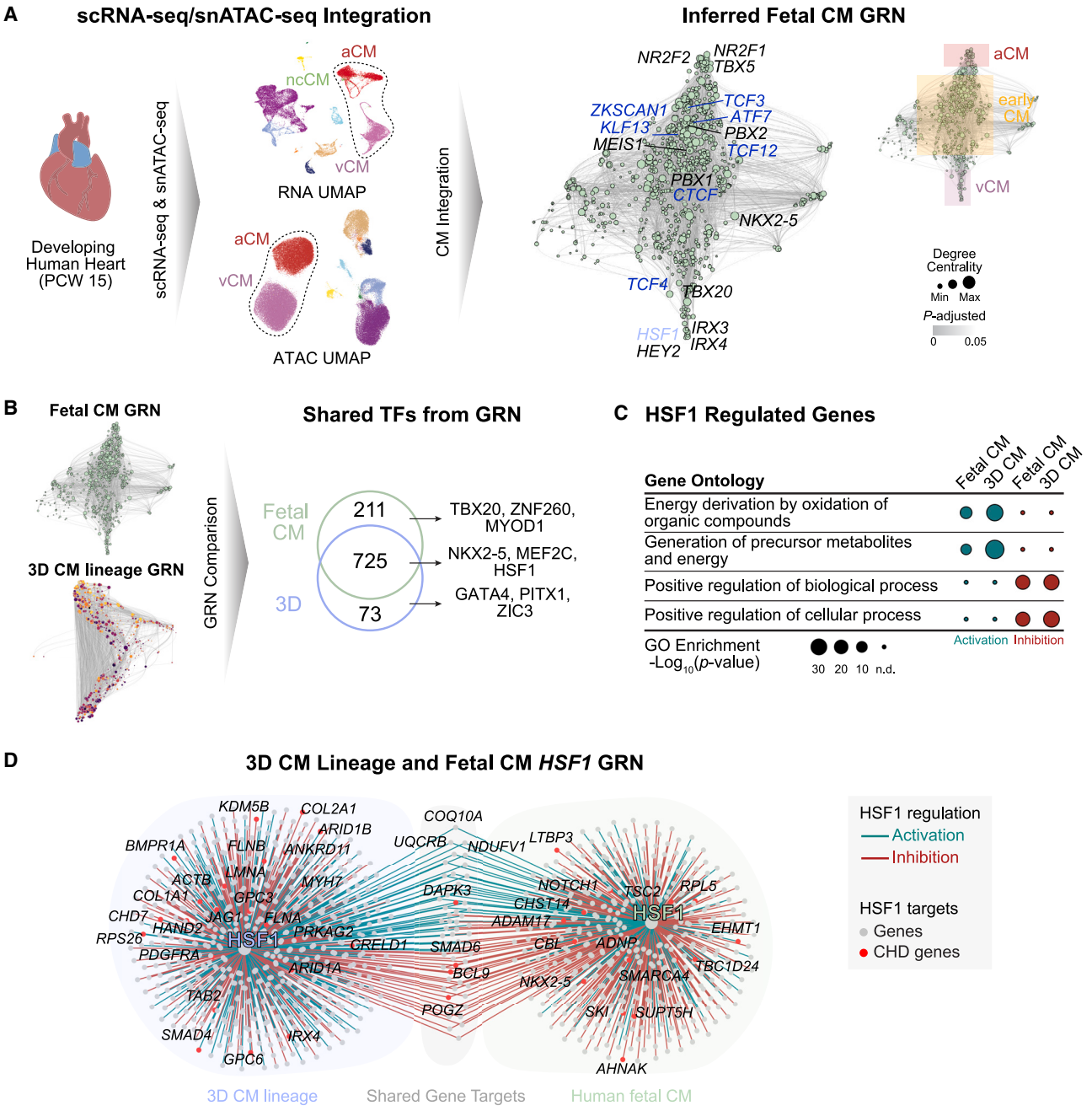


**Figure 6. HSF1 is a potential transcriptional regulator of cardiometabolic gene programs in the developing human heart**

(A) Schematic of strategy for scRNA-seq and snATAC-seq of human hearts for analyzing *in vivo* CMs. Dotted lines outline the cells utilized in building the CM-specific GRN. UMAP embedding of the inferred human fetal CM GRN based on correlation between TFs (right). UMAP embedding in top right is shaded by CM cell population specificity.

(B) Comparison between human fetal CM and 3D CM lineage GRNs identifies a high number of shared TFs between GRNs.

(C) GO terms for *HSF1* GRNs in 3D CM lineage and human fetal CMs show shared gene functions in activated (green) and inhibited (red) genes.

(D) Intersection of 3D CM lineage and human fetal CM GRNs specific for *HSF1* reveals a significant enrichment of CHD genes (red) in the 3D hPSC-CM lineage ($p = 3.52 \times 10^{-5}$) and human fetal CM *HSF1* GRNs ($p = 1.02^{-3}$) based on a Fisher's exact test. Activated and inhibited gene regulation represented in green and red, respectively.

PCW, post conception weeks; ncCM, non-chambered cardiomyocyte; n.d., no difference.

See also Figure S6.

known cardiac regulators with high degree centrality, including TBX5[33,34] and ESRRA,[130–132] illustrating the interconnectedness of these TFs within the GRN (Figure S6F; Table S5). Additionally, by visualizing the GRN using a UMAP embedding, we identified three distinct groups of TFs, (1) NR2F2 and NR2F1; (2) IRX3, IRX4, and HEY2; and (3) PBX1, PBX2, and MEIS1, that were associated with atrial (aCM), ventricular CM (vCM), and early CM development, respectively (Figure 6A). Notably, HSF1, a top regulator in the 3D hPSC-CM lineage GRN (Figure S4J), also grouped with the vCM TFs in the fetal CM GRN (Figure 6A), suggesting that HSF1 may regulate genes involved in vCM functionality *in vivo*. By contrast, many 2D-hPSC system-specific TFs grouped with early CM developmental TFs in the fetal CM GRN (Figure 6A). We then analyzed the human fetal CM GRN with the 2D and 3D hPSC-CM lineage GRNs to compare gene regulation among different populations of CMs and discovered that the majority of TF regulators between these GRNs were shared, including known TFs (e.g., ESRRG, TBX5) (Figure S6G). Additionally, the 3D hPSC-CM lineage GRN shared more TF regulators and regulated genes with the human fetal CM GRN than the 2D hPSC-CM lineage GRN, supporting a greater similarity between the 3D hPSC-CM lineage and human fetal CM GRNs (Figures 6B, S6G, and S6H). Consistent with these findings and the maturity of 3D hPSC-CMs, the transcriptomic profiles of human fetal CMs from 9 to 15 PCW[99] more closely resemble those from 3D hPSC-CMs than 2D hPSC-CMs (Figure S6I; Table S5).

Given this alignment in transcriptomic profiles, we next investigated whether HSF1 displays a similar role in both *in vitro* and *in vivo* human CMs by analyzing their inferred GRNs for HSF1. Based on GO terms, HSF1 was predicted to function as an activator of metabolic genes and an inhibitor of non-specific cellular process genes *in vitro* and *in vivo* (Figure 6C; Table S5). Interrogating HSF1 GRNs between human fetal CM and 3D hPSC-CM lineages revealed shared HSF1 gene targets, including the activation of genes (e.g., *COQ10A*, *UQCRB*, and *NDUFV1*) functioning in oxidative phosphorylation and metabolite generation (Figure 6D; Table S5). Since we identified HSF1 as a potential regulator of early cardiac developmental genes, we investigated whether HSF1 may be involved in CHD. While there are no known *HSF1* mutations in patients with CHD[133] (Table S5), our GRNs revealed that HSF1 target genes were implicated in CHD based on published datasets.[67] There were statistically more CHD-associated genes enriched in the 3D hPSC-CM lineage ($p = 3.52 \times 10^{-5}$) and human fetal CM HSF1 GRNs ($p = 1.02 \times 10^{-3}$) than expected by chance, based on a Fisher's exact test (Figure 6D), corroborating the importance of HSF1 in human cardiac development. Moreover, HSF1 target genes within the 3D hPSC-CM lineage and human fetal CM GRNs were also statistically enriched in genes associated with heart rate and hypertrophic cardiomyopathy (Table S5), thus supporting the role of HSF1 and its regulatory network in influencing broader cardiac traits. Thus, HSF1 is a vital cardiometabolic regulator within *in vitro* 3D-hPSC and human fetal CMs.

## DISCUSSION

Substantial efforts have been devoted to understanding how distinct cardiac cell types, including CMs, emerge from cardiac developmental sources.[134,135] Although prior studies have begun to illuminate the lineage relationships between cardiac progenitors and their differentiated cell types,[56,136] and the role of some specific genes regulating their development,[106,137–140] the underlying GRNs coordinating molecular programs directing cell fate decisions of cardiac progenitors into CMs remains to be fully elucidated. Thus, to address this crucial question, we combined multi-modal integrative single-cell analyses with high-throughput genomic studies to illuminate GRN dynamics and their corresponding TFs, which direct human cardiac development.

From these single-cell studies, we identified and organized cell populations participating in the developmental transitions of hPSCs into CMs. This hierarchical organization during CM development enabled lineage progression analysis to reveal not only the developmental history of CM lineages but also the genetic networks guiding their differentiation. We discovered distinct developmental trajectories between CM lineages generated from 2D Wnt-based and 3D BMP/ActA-based CM differentiation systems. Notably, these trajectories branched early during CM development, potentially leading to cellular differences between CMs from these systems as observed.[91–93]

Through our integrative GRN analyses combining scRNA-seq with snATAC-seq and organized by developmental pseudotime, we uncovered the coordinated gene regulatory programs directing intermediate cell fate decisions during CM development from these differentiation systems, as well as the TFs directing these GRNs. We identified well-known regulators of CM development shared between the two CM lineage trajectories including those in the MEIS and PBX TF families, which function cooperatively during heart development[141–143] and CHD.[144] Additionally, we discovered other known TFs specific for each CM lineage trajectory. TEAD1, -2, and -4 TFs, which regulate cardiac proliferation,[145–148] were observed in the 2D-hPSC system, whereas previously identified cardiac lineage-determining factors such as MEF2C[30–32] were present in the 3D-hPSC system. Furthermore, we discovered TFs with less recognized roles in cardiac function regulating these cardiac GRNs. For instance, AP-1-related TFs, predicted to regulate genes involved in cell proliferation, were identified in the 2D-hPSC system, and HSF1, predicted to regulate genes involved in metabolite generation, was detected in the 3D-hPSC system. Notably, TEAD family and AP-1-related factors, shown to synergistically regulate cell cycle target genes,[149,150] specifically coordinate GRNs in the 2D hPSC-CM system, which displayed increased CM proliferation.

While our GRN analyses revealed potential TFs directing these GRNs, our high-throughput functional genomic screen validated which of these TFs may be functionally significant for CM development within each cardiac differentiation system. In the CRISPR-Cas9 screen using the Wnt-based 2D hPSC-CM differentiation system, we identified TCF4 and TCF7L2, involved in the Wnt/β-catenin pathway and the initiation of the development of the mesendoderm,[116,117] a cell population observed in the 2D but not the 3D hPSC-CM system. Our GRN analysis revealed that TCF4 and TCF7L2 were also predicted to regulate *TEAD1* and *JUN*, respectively, controlling GRNs specific to the 2D hPSC-CM system. For 3D hPSC-CM differentiation, essential TFs identified from our 3D hPSC-CM screen included known

cardiac reprogramming factors, such as GATA4 and MEF2C,[151–153] as well as HSF1, a less recognized TF in CM development.

Our GRN analysis and experimental studies revealed that HSF1 may be crucial for regulating metabolic genes and CM metabolism. Additionally, loss of *HSF1* function in 3D hPSC-CMs results in cardiac mitochondrial and metabolism defects, phenocopying some of the 2D hPSC-CM metabolic phenotype (compare Figures 1F–1I to Figures 5D, 5F, S5J, and S5K), and impairs CM survival, highlighting the importance of metabolism in CM development and maturation.[47,88,154,155] Supporting the critical role of HSF1 in CM development, we discovered that target genes regulated by HSF1 are implicated as CHD candidate genes. Given the role of HSF1, along with GATA4 and MEF2C, in hPSC-CM development, these findings suggest that adding HSF1 to known cardiac lineage-determining factors including GATA4, MEF2C, and TBX5 may aid in reprogramming hPSCs and fibroblasts into durable adult-like CMs for potential therapeutic use.

Overall, these findings reveal the precise gene regulatory programs and essential TFs guiding the dynamic events during the development of stem cells into human CMs, including gene regulatory differences underlying the functional disparity between CMs from different *in vitro* cardiac systems. However, as human cardiac *in vitro* models progress, our single-cell genomic-based GRN and functional genomic screening strategies may be employed to investigate the gene programs and TFs governing CM differentiation into specific subpopulations (e.g., aCMs, vCMs, etc.), facilitating reprogramming strategies to treat cardiac diseases. Finally, while such information may be used to develop highly functional CMs for cardiac regenerative therapies, they may be also valuable for understanding early human cardiac development and pathologic mechanisms underlying CHD.

### Limitations of the study

Our studies focused on the early aspects of hPSC-CM development (day 25 or less) and may be limited in discovering gene regulatory programs directing later events, including differentiation into specific CM subtypes (i.e., aCMs and vCMs) and maturation at later time points. Furthermore, our study focused on identifying essential TFs that promote CM differentiation but may have limitations in uncovering functionally redundant TFs. Moreover, we have shown that HSF1 may be required in regulating metabolic gene programs; however, *HSF1* overexpression may not be sufficient to drive a comprehensive maturation process similar to 3D hPSC-CMs. Lastly, additional studies may be necessary to validate how GRNs and TFs coordinate human CM development *in vivo*, as our study primarily utilized *in vitro* hPSC systems.

## RESOURCE AVAILABILITY

### Lead contact

Further information and requests for resources and reagents should be directed to and will be fulfilled by the lead contact, Neil C. Chi (nchi@health.ucsd.edu).

### Materials availability

All unique reagents generated in this study are available from the lead contact with a completed materials transfer agreement.

### Data and code availability

- Raw sequencing data for the *in vitro* single-cell, CRISPR-Cas9 screen, and bulk RNA-seq studies have been deposited at GEO or to CIRM CESCG, and raw data for the human fetal single-cell studies have been deposited at dbGAP; all are publicly available as of the date of publication. Accession numbers are listed in the key resources table. Original western blot images have been deposited at Mendeley and will be publicly available as of the date of publication. The DOI is listed in the key resources table. Microscopy data reported in the paper will be shared by the lead contact upon request.
- All original code has been deposited at GitHub and will be publicly available as of the date of publication. Links are listed in the key resources table.
- Any additional information required to reanalyze the data reported in this paper is available from the lead contact upon request.

## ACKNOWLEDGMENTS

The authors thank Yoshitake Cho for assistance with Seahorse studies, the Chi and Engler laboratories for comments, and the UCSD core facilities: the Institute for Genomic Medicine for sequencing and the Human Embryonic Stem Cell Core Facility for cell sorting and analysis. The authors acknowledge funding and equipment support, in part, by grants from the National Institutes of Health to A.J.E. (R01AG045428), and N.C.C. Fellowship support was provided by the American Heart Association (20PRE35180060) to A.C.N. and the National Institutes of Health (F31HL163996 and T32GM008666) to A.R.H.

## AUTHOR CONTRIBUTIONS

A.R.H. and N.C.C. conceived the study, interpreted the data, and wrote the manuscript. A.R.H., E.D., E.N.F., T.L., and A.C.N. performed experiments and data analysis. A.R.H. and S.T. analyzed sequencing data. A.J.E. contributed to experimental design and results interpretation. S.T., E.D., E.N.F., and A.J.E. contributed to manuscript editing and discussion.

## DECLARATION OF INTERESTS

The authors declare no competing interests.

## STAR★METHODS

Detailed methods are provided in the online version of this paper and include the following:

- KEY RESOURCES TABLE
- EXPERIMENTAL MODEL AND STUDY PARTICIPANT DETAILS
  - HEK293T cells
  - hPSCs
  - Generation of an H9 HSF1 KO cell line
  - Human fetal heart tissues
- METHOD DETAILS
  - Experimental procedures
  - Data analysis
- QUANTIFICATION AND STATISTICAL ANALYSIS

## SUPPLEMENTAL INFORMATION

Supplemental information can be found online at https://doi.org/10.1016/j.xgen.2024.100680.

Received: May 1, 2024
Revised: August 1, 2024
Accepted: September 23, 2024
Published: October 21, 2024

## REFERENCES


1. Später, D., Hansson, E.M., Zangi, L., and Chien, K.R. (2014). How to make a cardiomyocyte. Development *141*, 4418–4431. https://doi.org/10.1242/DEV.091538.
2. Virani, S.S., Alonso, A., Benjamin, E.J., Bittencourt, M.S., Callaway, C.W., Carson, A.P., Chamberlain, A.M., Chang, A.R., Cheng, S., Delling, F.N., et al. (2020). Heart disease and stroke statistics—2020 update: A report from the American Heart Association at Lippincott Williams and Wilkins. https://doi.org/10.1161/CIR.0000000000000757.
3. Tzahor, E., and Lassar, A.B. (2001). Wnt signals from the neural tube block ectopic cardiogenesis. Genes Dev. *15*, 255–260. https://doi.org/10.1101/gad.871501.
4. Schneider, V.A., and Mercola, M. (2001). Wnt antagonism initiates cardiogenesis in Xenopus laevis. Genes Dev. *15*, 304–315. https://doi.org/10.1101/gad.855601.
5. Marvin, M.J., Di Rocco, G., Gardiner, A., Bush, S.M., and Lassar, A.B. (2001). Inhibition of Wnt activity induces heart formation from posterior mesoderm. Genes Dev. *15*, 316–327. https://doi.org/10.1101/gad.855501.
6. Schultheiss, T.M., Burch, J.B., and Lassar, A.B. (1997). A role for bone morphogenetic proteins in the induction of cardiac myogenesis. Genes Dev. *11*, 451–462. https://doi.org/10.1101/gad.11.4.451.
7. Yatskievych, T.A., Ladd, A.N., and Antin, P.B. (1997). Induction of cardiac myogenesis in avian pregastrula epiblast: The role of the hypoblast and activin. Development *124*, 2561–2570. https://doi.org/10.1242/dev.124.13.2561.
8. Ladd, A.N., Yatskievych, T.A., and Antin, P.B. (1998). Regulation of avian cardiac myogenesis by activin/TGFbeta and bone morphogenetic proteins. Dev. Biol. *204*, 407–419. https://doi.org/10.1006/DBIO.1998.9094.
9. Haegel, H., Larue, L., Ohsugi, M., Fedorov, L., Herrenknecht, K., and Kemler, R. (1995). Lack of β-catenin affects mouse development at gastrulation. Development *121*, 3529–3537. https://doi.org/10.1242/DEV.121.11.3529.
10. Rivera-Pérez, J.A., and Magnuson, T. (2005). Primitive streak formation in mice is preceded by localized activation of Brachyury and Wnt3. Dev. Biol. *288*, 363–371. https://doi.org/10.1016/J.YDBIO.2005.09.012.
11. Klaus, A., Saga, Y., Taketo, M.M., Tzahor, E., and Birchmeier, W. (2007). Distinct roles of Wnt/β-catenin and Bmp signaling during early cardiogenesis. Proc. Natl. Acad. Sci. USA *104*, 18531–18536. https://doi.org/10.1073/PNAS.0703113104.
12. Mishina, Y., Suzuki, A., Ueno, N., and Behringer, R.R. (1995). Bmpr encodes a type I bone morphogenetic protein receptor that is essential for gastrulation during mouse embryogenesis. Genes Dev. *9*, 3027–3037. https://doi.org/10.1101/gad.9.24.3027.
13. Parameswaran, M., and Tam, P.P. (1995). Regionalisation of cell fate and morphogenetic movement of the mesoderm during mouse gastrulation. Dev. Genet. *17*, 16–28. https://doi.org/10.1002/DVG.1020170104.
14. Lopez-Sanchez, C., Garcia-Martinez, V., and Schoenwolf, G.C. (2001). Localization of Cells of the Prospective Neural Plate, Heart and Somites within the Primitive Streak and Epiblast of Avian Embryos at Intermediate Primitive-Streak Stages. Cells Tissues Organs *169*, 334–346. https://doi.org/10.1159/000047900.
15. Yamaguchi, T.P., Takada, S., Yoshikawa, Y., Wu, N., and McMahon, A.P. (1999). T (Brachyury) is a direct target of Wnt3a during paraxial mesoderm specification. Genes Dev. *13*, 3185–3190. https://doi.org/10.1101/gad.13.24.3185.
16. Herrmann, B.G., Labeit, S., Poustka, A., King, T.R., and Lehrach, H. (1990). Cloning of the T gene required in mesoderm development in the mouse. Nature *343*, 617–622.
17. Costello, I., Pimeisl, I.M., Dräger, S., Bikoff, E.K., Robertson, E.J., and Arnold, S.J. (2011). The T-box transcription factor Eomesodermin acts upstream of Mesp1 to specify cardiac mesoderm during mouse gastrulation. Nat. Cell Biol. *139*, 1084–1091. https://doi.org/10.1038/ncb2304.
18. Van Den Ameele, J., Tiberi, L., Bondue, A., Paulissen, C., Herpoel, A., Iacovino, M., Kyba, M., Blanpain, C., and Vanderhaeghen, P. (2012). Eomesodermin induces Mesp1 expression and cardiac differentiation from embryonic stem cells in the absence of Activin. EMBO Rep. *13*, 355–362. https://doi.org/10.1038/EMBOR.2012.23.
19. Kitajima, S., Takagi, A., Inoue, T., and Saga, Y. (2000). MesP1 and MesP2 are essential for the development of cardiac mesoderm. Development *127*, 3215–3226. https://doi.org/10.1242/DEV.127.15.3215.
20. Saga, Y., Kitajima, S., and Miyagawa-Tomita, S. (2000). Mesp1 expression is the earliest sign of cardiovascular development. Trends Cardiovasc. Med. *10*, 345–352. https://doi.org/10.1016/S1050-1738(01)00069-X.
21. Saga, Y., Miyagawa-Tomita, S., Takagi, A., Kitajima, S., Miyazaki, J.I., and Inoue, T. (1999). MesP1 is expressed in the heart precursor cells and required for the formation of a single heart tube. Development *126*, 3437–3447. https://doi.org/10.1242/DEV.126.15.3437.
22. Lints, T.J., Parsons, L.M., Hartley, L., Lyons, I., and Harvey, R.P. (1993). Nkx-2.5: a novel murine homeobox gene expressed in early heart progenitor cells and their myogenic descendants. Development *119*, 419–431. https://doi.org/10.1242/DEV.119.2.419.
23. Lyons, I., Parsons, L.M., Hartley, L., Li, R., Andrews, J.E., Robb, L., and Harvey, R.P. (1995). Myogenic and morphogenetic defects in the heart tubes of murine embryos lacking the homeo box gene Nkx2-5. Genes Dev. *9*, 1654–1666. https://doi.org/10.1101/gad.9.13.1654.
24. Bodmer, R. (1993). The gene tinman is required for specification of the heart and visceral muscles in Drosophila. Development *118*, 719–729. https://doi.org/10.1242/dev.118.3.719.
25. Morrisey, E.E., Ip, H.S., Tang, Z., Lu, M.M., and Parmacek, M.S. (1997). GATA-5: A transcriptional activator expressed in a novel temporally and spatially-restricted pattern during embryonic development. Dev. Biol. *183*, 21–36. https://doi.org/10.1006/dbio.1996.8485.
26. Laverriere, A.C., Macneills, C., Muellero, C., Poelmann, R.E., Burch, J.B.E., and Evan, T. (1994). GATA-4/5/6, a Subfamily of Three Transcription Factors Transcribed in Developing Heart and Gut. J. Biol. Chem. *269*, 23177–23184.
27. Jiang, Y., and Evans, T. (1996). The Xenopus GATA-4/5/6 Genes Are Associated with Cardiac Specification and Can Regulate Cardiac-Specific Transcription during Embryogenesis. Dev. Biol. *174*, 258–270.
28. Morrisey, E.E., Ip, H.S., Lu, M.M., and Parmacek, M.S. (1996). GATA-6: A Zinc Finger Transcription Factor That Is Expressed in Multiple Cell Lineages Derived from Lateral Mesoderm. Dev. Biol. *177*, 309–322.
29. Heikinheimo, M., Scandrett, J.M., and Wilson, D.B. (1994). Localization of transcription factor GATA-4 to regions of the mouse embryo involved in cardiac development. Dev. Biol. *164*, 361–373.
30. Lin, Q., Schwarz, J., Bucana, C., and Olson, E.N. (1997). Control of mouse cardiac morphogenesis and myogenesis by transcription factor MEF2C. Science *276*, 1404–1407. https://doi.org/10.1126/SCIENCE.276.5317.1404.
31. Gossett, L.A., Kelvin, D.J., Sternberg, E.A., and Olson, E.N. (1989). A New Myocyte-Specific Enhancer-Binding Factor That Recognizes a Conserved Element Associated with Multiple Muscle-Specific. Mol. Cell Biol. *9*, 5022–5033. https://doi.org/10.1128/MCB.9.11.5022-5033.1989.
32. Edmondson, D.G., Lyons, G.E., Martin, J.F., and Olson, E.N. (1994). Mef2 gene expression marks the cardiac and skeletal muscle lineages during mouse embryogenesis. Development *120*, 1251–1263. https://doi.org/10.1242/dev.120.5.1251.
33. Basson, C.T., Bachinsky, D.R., Lin, R.C., Levi, T., Elkins, J.A., Soults, J., Grayzel, D., Kroumpouzou, E., Traill, T.A., Leblanc-Straceski, J., et al. (1997). Mutations in human cause limb and cardiac malformation in

Holt-Oram syndrome. Nat. Genet. *15*, 30–35. https://doi.org/10.1038/ng0197-30.

34. Bruneau, B.G., Logan, M., Davis, N., Levi, T., Tabin, C.J., Seidman, J.G., and Seidman, C.E. (1999). Chamber-specific cardiac expression of Tbx5 and heart defects in Holt-Oram syndrome. Dev. Biol. *211*, 100–108. https://doi.org/10.1006/DBIO.1999.9298.

35. Srivastava, D., Cserjesi, P., and Olson, E.N. (1995). A Subclass of bHLH Proteins Required for Cardiac Morphogenesis. Science *270*, 1995–1999. https://doi.org/10.1126/SCIENCE.270.5244.1995.

36. Tsuchihashi, T., Maeda, J., Shin, C.H., Ivey, K.N., Black, B.L., Olson, E.N., Yamagishi, H., and Srivastava, D. (2011). Hand2 function in second heart field progenitors is essential for cardiogenesis. Dev. Biol. *351*, 62–69. https://doi.org/10.1016/j.ydbio.2010.12.023.

37. Barnes, R.M., Firulli, B.A., Vandusen, N.J., Morikawa, Y., Conway, S.J., Cserjesi, P., Vincentz, J.W., and Firulli, A.B. (2011). Hand2 loss-of-function in hand1-expressing cells reveals distinct roles in epicardial and coronary vessel development. Circ. Res. *108*, 940–949. https://doi.org/10.1161/CIRCRESAHA.110.233171.

38. Firulli, B.A., Howard, M.J., McDaid, J.R., McIlreavey, L., Dionne, K.M., Centonze, V.E., Cserjesi, P., Virshup, D.M., and Firulli, A.B. (2003). PKA, PKC, and the protein phosphatase 2A influence HAND factor function: A mechanism for tissue-specific transcriptional regulation. Mol. Cell *12*, 1225–1237. https://doi.org/10.1016/S1097-2765(03)00425-8.

39. Cai, C.L., Liang, X., Shi, Y., Chu, P.H., Pfaff, S.L., Chen, J., and Evans, S. (2003). Isl1 Identifies a Cardiac Progenitor Population that Proliferates Prior to Differentiation and Contributes a Majority of Cells to the Heart. Dev. Cell *5*, 877–889. https://doi.org/10.1016/S1534-5807(03)00363-0.

40. Zhang, Y., Zhang, Y., Song, C., Zhao, X., Ai, B., Wang, Y., Zhou, L., Zhu, J., Feng, C., Xu, L., et al. (2023). CRdb: a comprehensive resource for deciphering chromatin regulators in human. Nucleic Acids Res. *51*, D88–D100. https://doi.org/10.1093/nar/gkac960.

41. Zaidi, S., Choi, M., Wakimoto, H., Ma, L., Jiang, J., Overton, J.D., Romano-Adesman, A., Bjornson, R.D., Breitbart, R.E., Brown, K.K., et al. (2013). De novo mutations in histone modifying genes in congenital heart disease. Nature *498*, 220–223. https://doi.org/10.1038/NATURE12141.

42. Zhang, Y., Song, C., Zhang, Y., Wang, Y., Feng, C., Chen, J., Wei, L., Pan, Q., Shang, D., Zhu, Y., et al. (2022). TcoFBase: A comprehensive database for decoding the regulatory transcription co-factors in human and mouse. Nucleic Acids Res. *50*, D391–D401. https://doi.org/10.1093/nar/gkab950.

43. Vincent, S.D., and Buckingham, M.E. (2010). How to Make a Heart: The Origin and Regulation of Cardiac Progenitor Cells. Curr. Top. Dev. Biol. *90*, 1–41. https://doi.org/10.1016/S0070-2153(10)90001-X.

44. Fahed, A.C., Gelb, B.D., Seidman, J.G., and Seidman, C.E. (2013). Genetics of congenital heart disease: The glass half empty. Circ. Res. *112*, 707–720. https://doi.org/10.1161/CIRCRESAHA.112.300853.

45. Jin, S.C., Homsy, J., Zaidi, S., Lu, Q., Morton, S., Depalma, S.R., Zeng, X., Qi, H., Chang, W., Sierant, M.C., et al. (2017). Contribution of rare inherited and de novo variants in 2,871 congenital heart disease probands. Nat. Genet. *49*, 1593–1601. https://doi.org/10.1038/ng.3970.

46. Homsy, J., Zaidi, S., Shen, Y., Ware, J.S., Samocha, K.E., Karczewski, K.J., Depalma, S.R., Mckean, D., Wakimoto, H., Gorham, J., et al. (2015). De novo mutations in congenital heart disease with neurodevelopmental and Other Congenital Anomalies. Science *350*, 1262–1266.

47. DeLaughter, D.M., Bick, A.G., Wakimoto, H., McKean, D., Gorham, J.M., Kathiriya, I.S., Hinson, J.T., Homsy, J., Gray, J., Pu, W., et al. (2016). Single-Cell Resolution of Temporal Gene Expression during Heart Development. Dev. Cell *39*, 480–490. https://doi.org/10.1016/j.devcel.2016.10.001.

48. Litviňuková, M., Talavera-López, C., Maatz, H., Reichart, D., Worth, C.L., Lindberg, E.L., Kanda, M., Polanski, K., Heinig, M., Lee, M., et al. (2020). Cells of the adult human heart. Nature *588*, 466–472.

49. Tucker, N.R., Chaffin, M., Fleming, S.J., Hall, A.W., Parsons, V.A., Bedi, K.C., Akkad, A.D., Herndon, C.N., Arduini, A., Papangeli, I., et al. (2020). Transcriptional and Cellular Diversity of the Human Heart. Circulation *142*, 466–482. https://doi.org/10.1161/CIRCULATIONAHA.119.045401.

50. Cui, Y., Zheng, Y., Liu, X., Yan, L., Fan, X., Yong, J., Hu, Y., Dong, J., Li, Q., Wu, X., et al. (2019). Single-Cell Transcriptome Analysis Maps the Developmental Track of the Human Heart. Cell Rep. *26*, 1934–1950.e5. https://doi.org/10.1016/j.celrep.2019.01.079.

51. Ameen, M., Sundaram, L., Shen, M., Banerjee, A., Kundu, S., Nair, S., Shcherbina, A., Gu, M., Wilson, K.D., Varadarajan, A., et al. (2022). Integrative single-cell analysis of cardiogenesis identifies developmental trajectories and non-coding mutations in congenital heart disease. Cell *185*, 4937–4953.e23.

52. Hocker, J.D., Poirion, O.B., Zhu, F., Buchanan, J., Zhang, K., Chiou, J., Wang, T.M., Zhang, Q., Hou, X., Li, Y.E., et al. (2021). Cardiac cell type–specific gene regulatory programs and disease risk association. Sci. Adv. *7*, eabf1444.

53. Skelly, D.A., Squiers, G.T., Mclellan, M.A., Bolisetty, M.T., Robson, P., Rosenthal, N.A., and Pinto, A.R. (2018). Single-Cell Transcriptional Profiling Reveals Cellular Diversity and Intercommunication in the Mouse Heart. Cell Rep. *22*, 600–610. https://doi.org/10.1016/j.celrep.2017.12.072.

54. Lescroart, F., Wang, X., Lin, X., Swedlund, B., Gargouri, S., Sànchez-Dànes, A., Moignard, V., Dubois, C., Paulissen, C., Kinston, S., et al. (2018). Defining the earliest step of cardiovascular lineage segregation by single-cell RNA-seq. Science *359*, 1177–1181. https://doi.org/10.1126/SCIENCE.AAO4174.

55. Feng, W., Bais, A., He, H., Rios, C., Jiang, S., Xu, J., Chang, C., Kostka, D., and Li, G. (2022). Single-cell transcriptomic analysis identifies murine heart molecular features at embryonic and neonatal stages. Nat. Commun. *13*, 7960. https://doi.org/10.1038/s41467-022-35691-7.

56. Zhang, Q., Carlin, D., Zhu, F., Cattaneo, P., Ideker, T., Evans, S.M., Bloomekatz, J., and Chi, N.C. (2021). Unveiling Complexity and Multipotentiality of Early Heart Fields. Circ. Res. *129*, 474–487. https://doi.org/10.1161/CIRCRESAHA.121.318943.

57. Li, G., Xu, A., Sim, S., Priest, J.R., Tian, X., Khan, T., Quertermous, T., Zhou, B., Tsao, P.S., Quake, S.R., and Wu, S.M. (2016). Transcriptomic Profiling Maps Anatomically Patterned Subpopulations among Single Embryonic Cardiac Cells. Dev. Cell *39*, 491–507. https://doi.org/10.1016/j.devcel.2016.10.014.

58. Churko, J.M., Garg, P., Treutlein, B., Venkatasubramanian, M., Wu, H., Lee, J., Wessells, Q.N., Chen, S.Y., Chen, W.Y., Chetal, K., et al. (2018). Defining human cardiac transcription factor hierarchies using integrated single-cell heterogeneity analysis. Nat. Commun. *9*, 4906. https://doi.org/10.1038/s41467-018-07333-4.

59. Drakhlis, L., Biswanath, S., Farr, C.-M., Lupanow, V., Teske, J., Ritzenhoff, K., Franke, A., Manstein, F., Bolesani, E., Kempf, H., et al. (2021). Human heart-forming organoids recapitulate early heart and foregut development. Nat. Biotechnol. *39*, 737–746. https://doi.org/10.1038/s41587-021-00815-9.

60. Meier, A.B., Zawada, D., De Angelis, M.T., Martens, L.D., Santamaria, G., Zengerle, S., Nowak-Imialek, M., Kornherr, J., Zhang, F., Tian, Q., et al. (2023). Epicardioid single-cell genomics uncovers principles of human epicardium biology in heart development and disease. Nat. Biotechnol. *41*, 1787–1800. https://doi.org/10.1038/s41587-023-01718-7.

61. Yang, D., Gomez-Garcia, J., Funakoshi, S., Tran, T., Fernandes, I., Bader, G.D., Laflamme, M.A., and Keller, G.M. (2022). Modeling human multi-lineage heart field development with pluripotent stem cells. Cell Stem Cell *29*, 1382–1401.e8. https://doi.org/10.1016/J.STEM.2022.08.007.

62. Funakoshi, S., Fernandes, I., Mastikhina, O., Wilkinson, D., Tran, T., Dhahri, W., Mazine, A., Yang, D., Burnett, B., Lee, J., et al. (2021). Generation of mature compact ventricular cardiomyocytes from human

pluripotent stem cells. Nat. Commun. *12*, 3155. https://doi.org/10.1038/s41467-021-23329-z.

63. Mikryukov, A.A., Mazine, A., Wei, B., Yang, D., Miao, Y., Gu, M., and Keller, G.M. (2021). BMP10 Signaling Promotes the Development of Endocardial Cells from Human Pluripotent Stem Cell-Derived Cardiovascular Progenitors. Cell Stem Cell *28*, 96–111.e7. https://doi.org/10.1016/j.stem.2020.10.003.

64. Silva, A.C., Matthys, O.B., Joy, D.A., Kauss, M.A., Natarajan, V., Lai, M.H., Turaga, D., Blair, A.P., Alexanian, M., Bruneau, B.G., and McDevitt, T.C. (2021). Co-emergence of cardiac and gut tissues promotes cardiomyocyte maturation within human iPSC-derived organoids. Cell Stem Cell *28*, 2137–2152.e6. https://doi.org/10.1016/j.stem.2021.11.007.

65. Friedman, C.E., Nguyen, Q., Lukowski, S.W., Helfer, A., Chiu, H.S., Miklas, J., Levy, S., Suo, S., Han, J.D.J., Osteil, P., et al. (2018). Single-Cell Transcriptomic Analysis of Cardiac Differentiation from Human PSCs Reveals HOPX-Dependent Cardiomyocyte Maturation. Cell Stem Cell *23*, 586–598.e8. https://doi.org/10.1016/j.stem.2018.09.009.

66. Hofbauer, P., Jahnel, S.M., Papai, N., Giesshammer, M., Deyett, A., Schmidt, C., Penc, M., Tavernini, K., Grdseloff, N., Meledeth, C., et al. (2021). Cardioids reveal self-organizing principles of human cardiogenesis. Cell *184*, 3299–3317.e22. https://doi.org/10.1016/j.cell.2021.04.034.

67. Kathiriya, I.S., Rao, K.S., Iacono, G., Devine, W.P., Blair, A.P., Hota, S.K., Lai, M.H., Garay, B.I., Thomas, R., Gong, H.Z., et al. (2021). Modeling Human TBX5 Haploinsufficiency Predicts Regulatory Networks for Congenital Heart Disease. Dev. Cell *56*, 292–309.e9. https://doi.org/10.1016/j.devcel.2020.11.020.

68. Fleck, J.S., Jansen, S.M.J., Wollny, D., Zenk, F., Seimiya, M., Jain, A., Okamoto, R., Santel, M., He, Z., Camp, J.G., and Treutlein, B. (2023). Inferring and perturbing cell fate regulomes in human brain organoids. Nature *621*, 365–372. https://doi.org/10.1038/s41586-022-05279-8.

69. Bravo González-Blas, C., De Winter, S., Hulselmans, G., Hecker, N., Matetovici, I., Christiaens, V., Poovathingal, S., Wouters, J., Aibar, S., and Aerts, S. (2023). SCENIC+: single-cell multiomic inference of enhancers and gene regulatory networks. Nat. Methods *20*, 1355–1367. https://doi.org/10.1038/s41592-023-01938-4.

70. Kartha, V.K., Duarte, F.M., Hu, Y., Ma, S., Chew, J.G., Lareau, C.A., Earl, A., Burkett, Z.D., Kohlway, A.S., Lebofsky, R., and Buenrostro, J.D. (2022). Functional inference of gene regulation using single-cell multi-omics. Cell Genom. *2*, 100166. https://doi.org/10.1016/J.XGEN.2022.100166.

71. Kamal, A., Arnold, C., Claringbould, A., Moussa, R., Servaas, N.H., Kholmatov, M., Daga, N., Nogina, D., Mueller-Dott, S., Reyes-Palomares, A., et al. (2023). GRaNIE and GRaNPA: inference and evaluation of enhancer-mediated gene regulatory networks. Mol. Syst. Biol. *19*, e11627. https://doi.org/10.15252/MSB.202311627.

72. Badia-i-Mompel, P., Wessels, L., Müller-Dott, S., Trimbour, R., Ramirez Flores, R.O., Argelaguet, R., and Saez-Rodriguez, J. (2023). Gene regulatory network inference in the era of single-cell multi-omics. Nat. Rev. Genet. *24*, 739–754. https://doi.org/10.1038/s41576-023-00618-5.

73. Wang, T., Wei, J.J., Sabatini, D.M., and Lander, E.S. (2014). Genetic screens in human cells using the CRISPR-Cas9 system. Science *343*, 80–84. https://doi.org/10.1126/science.1246981.

74. Shalem, O., Sanjana, N.E., Hartenian, E., Shi, X., Scott, D.A., Mikkelson, T., Heckl, D., Ebert, B.L., Root, D.E., Doench, J.G., and Zhang, F. (2014). Genome-Scale CRISPR-Cas9 Knockout Screening in Human Cells. Science *343*, 84–87.

75. Joung, J., Ma, S., Tay, T., Geiger-Schuller, K.R., Kirchgatterer, P.C., Verdine, V.K., Guo, B., Arias-Garcia, M.A., Allen, W.E., Singh, A., et al. (2023). A transcription factor atlas of directed differentiation. Cell *186*, 209–229.e26. https://doi.org/10.1016/j.cell.2022.11.026.

76. VanDusen, N.J., Lee, J.Y., Gu, W., Butler, C.E., Sethi, I., Zheng, Y., King, J.S., Zhou, P., Suo, S., Guo, Y., et al. (2021). Massively parallel in vivo CRISPR screening identifies RNF20/40 as epigenetic regulators of cardiomyocyte maturation. Nat. Commun. *12*, 4442. https://doi.org/10.1038/s41467-021-24743-z.

77. Missinato, M.A., Murphy, S., Lynott, M., Yu, M.S., Kervadec, A., Chang, Y.L., Kannan, S., Loreti, M., Lee, C., Amatya, P., et al. (2023). Conserved transcription factors promote cell fate stability and restrict reprogramming potential in differentiated cells. Nat. Commun. *14*, 1709. https://doi.org/10.1038/s41467-023-37256-8.

78. Gonzalez, G., Holman, A.R., Nelson, A.C., and Engler, A.J. (2022). Engineering the niche to differentiate and deploy cardiovascular cells. Curr. Opin. Biotechnol. *74*, 122–128. https://doi.org/10.1016/j.copbio.2021.11.003.

79. Lian, X., Bao, X., Zilberter, M., Westman, M., Fisahn, A., Hsiao, C., Hazeltine, L.B., Dunn, K.K., Kamp, T.J., and Palecek, S.P. (2015). Chemically defined, albumin-free human cardiomyocyte generation. Nat. Methods *12*, 595–596, at Nature Publishing Group. https://doi.org/10.1038/nmeth.3448.

80. Kattman, S.J., Witty, A.D., Gagliardi, M., Dubois, N.C., Niapour, M., Hotta, A., Ellis, J., and Keller, G. (2011). Stage-specific optimization of activin/nodal and BMP signaling promotes cardiac differentiation of mouse and human pluripotent stem cell lines. Cell Stem Cell *8*, 228–240. https://doi.org/10.1016/j.stem.2010.12.008.

81. Lian, X., Hsiao, C., Wilson, G., Zhu, K., Hazeltine, L.B., Azarin, S.M., Raval, K.K., Zhang, J., Kamp, T.J., and Palecek, S.P. (2012). Robust cardiomyocyte differentiation from human pluripotent stem cells via temporal modulation of canonical Wnt signaling. Proc. Natl. Acad. Sci. USA *109*, E1848–E1857. https://doi.org/10.1073/pnas.1200250109.

82. Lee, J.H., Protze, S.I., Laksman, Z., Backx, P.H., and Keller, G.M. (2017). Human Pluripotent Stem Cell-Derived Atrial and Ventricular Cardiomyocytes Develop from Distinct Mesoderm Populations. Cell Stem Cell *21*, 179–194.e4. https://doi.org/10.1016/j.stem.2017.07.003.

83. Wrighton, P.J., Klim, J.R., Hernandez, B.A., Koonce, C.H., Kamp, T.J., and Kiessling, L.L. (2014). Signals from the surface modulate differentiation of human pluripotent stem cells through glycosaminoglycans and integrins. Proc. Natl. Acad. Sci. USA *111*, 18126–18131. https://doi.org/10.1073/PNAS.1409525111.

84. Porrello, E.R., Mahmoud, A.I., Simpson, E., Hill, J.A., Richardson, J.A., Olson, E.N., and Sadek, H.A. (2011). Transient regenerative potential of the neonatal mouse heart. Science *331*, 1078–1080. https://doi.org/10.1126/science.1200708.

85. Heidi Au, H.T., Cui, B., Chu, Z.E., Veres, T., and Radisic, M. (2009). Cell culture chips for simultaneous application of topographical and electrical cues enhance phenotype of cardiomyocytes. Lab Chip *9*, 564–575. https://doi.org/10.1039/b810034a.

86. Vermij, S.H., Abriel, H., and Van Veen, T.A.B. (2017). Refining the molecular organization of the cardiac intercalated disc. Cardiovasc. Res. *113*, 259–275. https://doi.org/10.1093/cvr/cvw259.

87. Piquereau, J., and Ventura-Clapier, R. (2018). Maturation of cardiac energy metabolism during perinatal development. Front. Physiol. *9*, 959. https://doi.org/10.3389/fphys.2018.00959.

88. Ascuitto, R.J., and Ross-Ascuitto, N.T. (1996). Substrate metabolism in the developing heart. Semin. Perinatol. *20*, 542–563. https://doi.org/10.1016/S0146-0005(96)80068-1.

89. Han, L., Huang, D., Wu, S., Liu, S., Wang, C., Sheng, Y., Lu, X., Broxmeyer, H.E., Wan, J., and Yang, L. (2023). Lipid droplet-associated lncRNA LIPTER preserves cardiac lipid metabolism. Nat. Cell Biol. *25*, 1033–1046. https://doi.org/10.1038/s41556-023-01162-4.

90. Glancy, B., Hartnell, L.M., Malide, D., Yu, Z.X., Combs, C.A., Connelly, P.S., Subramaniam, S., and Balaban, R.S. (2015). Mitochondrial reticulum for cellular energy distribution in muscle. Nature *523*, 617–620. https://doi.org/10.1038/NATURE14614.

91. Sacchetto, C., Vitiello, L., de Windt, L.J., Rampazzo, A., and Calore, M. (2020). Modeling Cardiovascular Diseases with hiPSC-Derived

Cardiomyocytes in 2D and 3D Cultures. Int. J. Mol. Sci. *21*, 3404. https://doi.org/10.3390/IJMS21093404.

92. Correia, C., Koshkin, A., Duarte, P., Hu, D., Carido, M., Sebastião, M.J., Gomes-Alves, P., Elliott, D.A., Domian, I.J., Teixeira, A.P., et al. (2018). 3D aggregate culture improves metabolic maturation of human pluripotent stem cell derived cardiomyocytes. Biotechnol. Bioeng. *115*, 630–644.
93. Pontes Soares, C., Midlej, V., de Oliveira, M.E.W., Benchimol, M., Costa, M.L., and Mermelstein, C. (2012). 2D and 3D-Organized Cardiac Cells Shows Differences in Cellular Morphology, Adhesion Junctions, Presence of Myofibrils and Protein Expression. PLoS One *7*, e38147. https://doi.org/10.1371/JOURNAL.PONE.0038147.
94. Zhang, Y., Li, T., Preissl, S., Amaral, M.L., Grinstein, J.D., Farah, E.N., Destici, E., Qiu, Y., Hu, R., Lee, A.Y., et al. (2019). Transcriptionally active HERV-H retrotransposons demarcate topologically associating domains in human pluripotent stem cells. Nat. Genet. *51*, 1380–1388. https://doi.org/10.1038/s41588-019-0479-7.
95. Destici, E., Zhu, F., Tran, S., Preissl, S., Farah, E.N., Zhang, Y., Hou, X., Poirion, O.B., Lee, A.Y., Grinstein, J.D., et al. (2022). Human-gained heart enhancers are associated with species-specific cardiac attributes. Nat. Cardiovasc. Res. *1*, 830–843. https://doi.org/10.1038/s44161-022-00124-7.
96. Hao, Y., Hao, S., Andersen-Nissen, E., Mauck, W.M., Zheng, S., Butler, A., Lee, M.J., Wilk, A.J., Darby, C., Zager, M., et al. (2021). Integrated analysis of multimodal single-cell data. Cell *184*, 3573–3587.e29. https://doi.org/10.1016/J.CELL.2021.04.048.
97. Granja, J.M., Corces, M.R., Pierce, S.E., Bagdatli, S.T., Choudhry, H., Chang, H.Y., and Greenleaf, W.J. (2021). Author Correction: ArchR is a scalable software package for integrative single-cell chromatin accessibility analysis. Nat. Genet. *53*, 935. https://doi.org/10.1038/s41588-021-00850-x.
98. Tyser, R.C.V., Mahammadov, E., Nakanoh, S., Vallier, L., Scialdone, A., and Srinivas, S. (2021). Single cell transcriptomic characterization of a gastrulating human embryo. Nature *600*, 285–289. https://doi.org/10.1038/S41586-021-04158-Y.
99. Farah, E.N., Hu, R.K., Kern, C., Zhang, Q., Lu, T.-Y., Ma, Q., Tran, S., Zhang, B., Carlin, D., Monell, A., et al. (2024). Spatially organized cellular communities form the developing human heart. Nature *627*, 854–864. https://doi.org/10.1038/s41586-024-07171-z.
100. Chen, H., Lareau, C., Andreani, T., Vinyard, M.E., Garcia, S.P., Clement, K., Andrade-Navarro, M.A., Buenrostro, J.D., and Pinello, L. (2019). Assessment of computational methods for the analysis of single-cell ATAC-seq data. Genome Biol. *20*, 241. https://doi.org/10.1186/s13059-019-1854-5.
101. Cusanovich, D.A., Hill, A.J., Aghamirzaie, D., Daza, R.M., Pliner, H.A., Berletch, J.B., Filippova, G.N., Huang, X., Christiansen, L., DeWitt, W.S., et al. (2018). A Single-Cell Atlas of In Vivo Mammalian Chromatin Accessibility. Cell *174*, 1309–1324.e18. https://doi.org/10.1016/j.cell.2018.06.052.
102. Lake, B.B., Chen, S., Sos, B.C., Fan, J., Kaeser, G.E., Yung, Y.C., Duong, T.E., Gao, D., Chun, J., Kharchenko, P.V., and Zhang, K. (2018). Integrative single-cell analysis of transcriptional and epigenetic states in the human adult brain. Nat. Biotechnol. *36*, 70–80. https://doi.org/10.1038/nbt.4038.
103. Farrell, J.A., Wang, Y., Riesenfeld, S.J., Shekhar, K., Regev, A., and Schier, A.F. (2018). Single-cell reconstruction of developmental trajectories during zebrafish embryogenesis. Science *360*, eaar3131. https://doi.org/10.1126/science.aar3131.
104. Laurent, F., Girdziusaite, A., Gamart, J., Barozzi, I., Osterwalder, M., Akiyama, J.A., Lincoln, J., Lopez-Rios, J., Visel, A., Zuniga, A., and Zeller, R. (2017). HAND2 Target Gene Regulatory Networks Control Atrioventricular Canal and Cardiac Valve Development. Cell Rep. *19*, 1602–1613. https://doi.org/10.1016/j.celrep.2017.05.004.
105. von Both, I., Silvestri, C., Erdemir, T., Lickert, H., Walls, J.R., Henkelman, R.M., Rossant, J., Harvey, R.P., Attisano, L., and Wrana, J.L. (2004). Foxh1 Is Essential for Development of the Anterior Heart Field. Dev. Cell *7*, 331–345. https://doi.org/10.1016/J.DEVCEL.2004.07.023.
106. Dodou, E., Verzi, M.P., Anderson, J.P., Xu, S.M., and Black, B.L. (2004). Mef2c is a direct transcriptional target of ISL1 and GATA factors in the anterior heart field during mouse embryonic development. Development *131*, 3931–3942. https://doi.org/10.1242/dev.01256.
107. Bruneau, B.G., Nemer, G., Schmitt, J.P., Charron, F., Robitaille, L., Caron, S., Conner, D.A., Gessler, M., Nemer, M., Seidman, C.E., and Seidman, J.G. (2001). A Murine Model of Holt-Oram Syndrome Defines Roles of the T-Box Transcription Factor Tbx5 in Cardiogenesis and Disease. Cell *106*, 709–721. https://doi.org/10.1016/S0092-8674(01)00493-7.
108. Zhang, H., Zhang, Y., Zhou, X., Wright, S., Hyle, J., Zhao, L., An, J., Zhao, X., Shao, Y., Xu, B., et al. (2020). Functional interrogation of HOXA9 regulome in MLLr leukemia via reporter-based CRISPR/Cas9 screen. Elife *9*, e57858. https://doi.org/10.7554/ELIFE.57858.
109. Han, C.R., Wang, H., Hoffmann, V., Zerfas, P., Kruhlak, M., and Cheng, S.Y. (2021). Thyroid Hormone Receptor $\alpha$ Mutations Cause Heart Defects in Zebrafish. Thyroid *31*, 315–326. https://doi.org/10.1089/thy.2020.0332.
110. Mitsui, K., Tokuzawa, Y., Itoh, H., Segawa, K., Murakami, M., Takahashi, K., Maruyama, M., Maeda, M., and Yamanaka, S. (2003). The homeoprotein nanog is required for maintenance of pluripotency in mouse epiblast and ES cells. Cell *113*, 631–642. https://doi.org/10.1016/S0092-8674(03)00393-3.
111. Reginensi, A., Clarkson, M., Neirijnck, Y., Lu, B., Ohyama, T., Groves, A.K., Sock, E., Wegner, M., Costantini, F., Chaboissier, M.C., and Schedl, A. (2011). SOX9 controls epithelial branching by activating RET effector genes during kidney development. Hum. Mol. Genet. *20*, 1143–1153. https://doi.org/10.1093/HMG/DDQ558.
112. Müller, T., Anlag, K., Wildner, H., Britsch, S., Treier, M., and Birchmeier, C. (2005). The bHLH factor Olig3 coordinates the specification of dorsal neurons in the spinal cord. Genes Dev. *19*, 733–743. https://doi.org/10.1101/gad.326105.
113. MacDonald, B.T., Tamai, K., and He, X. (2009). Wnt/β-Catenin Signaling: Components, Mechanisms, and Diseases. Dev. Cell *17*, 9–26. https://doi.org/10.1016/j.devcel.2009.06.016.
114. Kim, K.H., Rosen, A., Hussein, S.M.I., Puviindran, V., Korogyi, A.S., Chiarello, C., Nagy, A., Hui, C.C., and Backx, P.H. (2016). Irx3 is required for postnatal maturation of the mouse ventricular conduction system. Sci. Rep. *6*, 19197–19214. https://doi.org/10.1038/srep19197.
115. Canac, R., Cimarosti, B., Girardeau, A., Forest, V., Olchesqui, P., Poschmann, J., Redon, R., Lemarchand, P., Gaborit, N., and Lamirault, G. (2022). Deciphering transcriptional networks during human cardiac development. Cells *11*, 3915. https://doi.org/10.1101/2022.08.11.503560.
116. Yang, J., Tan, C., Darken, R.S., Wilson, P.A., and Klein, P.S. (2002). β-catenin/Tcf-regulated transcription prior to the midblastula transition. Development *129*, 5743–5752. https://doi.org/10.1242/dev.00150.
117. Houston, D.W., Kofron, M., Resnik, E., Langland, R., Destree, O., Wylie, C., and Heasman, J. (2002). Repression of organizer genes in dorsal and ventral Xenopus cells mediated by maternal XTcf3. Development *129*, 4015–4025. https://doi.org/10.1242/dev.129.17.4015.
118. Potthoff, M.J., and Olson, E.N. (2007). MEF2: a central regulator of diverse developmental programs. Development *134*, 4131–4140. https://doi.org/10.1242/DEV.008367.
119. Black, B.L., and Olson, E.N. (1998). Transcriptional control of muscle development by myocyte enhancer factor-2 (MEF2) proteins. Annu. Rev. Cell Dev. Biol. *14*, 167–196. https://doi.org/10.1146/ANNUREV.CELLBIO.14.1.167.

120. Åkerfelt, M., Morimoto, R.I., and Sistonen, L. (2010). Heat shock factors: integrators of cell stress, development and lifespan. Nat. Rev. Mol. Cell Biol. *11*, 545–555. https://doi.org/10.1038/nrm2938.

121. Bierkamp, C., Luxey, M., Metchat, A., Audouard, C., Dumollard, R., and Christians, E. (2010). Lack of maternal Heat Shock Factor 1 results in multiple cellular and developmental defects, including mitochondrial damage and altered redox homeostasis, and leads to reduced survival of mammalian oocytes and embryos. Dev. Biol. *339*, 338–353. https://doi.org/10.1016/J.YDBIO.2009.12.037.

122. Yan, L.J., Christians, E.S., Liu, L., Xiao, X., Sohal, R.S., and Benjamin, I.J. (2002). Mouse heat shock transcription factor 1 deficiency alters cardiac redox homeostasis and increases mitochondrial oxidative damage. EMBO J. *21*, 5164–5172. https://doi.org/10.1093/EMBOJ/CDF528.

123. Gomez-Pastor, R., Burchfiel, E.T., and Thiele, D.J. (2018). Regulation of heat shock transcription factors and their roles in physiology and disease. Nat. Rev. Mol. Cell Biol. *19*, 4–19. https://doi.org/10.1038/nrm.2017.73.

124. Cui, T., Wang, Y., Song, P., Yi, X., Chen, J., Yang, Y., Wang, H., Kang, P., Guo, S., Liu, L., et al. (2022). HSF1-Dependent Autophagy Activation Contributes to the Survival of Melanocytes Under Oxidative Stress in Vitiligo. J. Invest. Dermatol. *142*, 1659–1669.e4. https://doi.org/10.1016/j.jid.2021.11.007.

125. Avilion, A.A., Nicolis, S.K., Pevny, L.H., Perez, L., Vivian, N., and Lovell-Badge, R. (2003). Multipotent cell lineages in early mouse development depend on SOX2 function. Genes Dev. *17*, 126–140. https://doi.org/10.1101/GAD.224503.

126. Mayr, F., and Heinemann, U. (2013). Mechanisms of Lin28-Mediated miRNA and mRNA Regulation-A Structural and Functional Perspective. Int. J. Mol. Sci. *14*, 16532–16553. https://doi.org/10.3390/ijms140816532.

127. Lee, H.Y., Choi, C.S., Birkenfeld, A.L., Alves, T.C., Jornayvaz, F.R., Jurczak, M.J., Zhang, D., Woo, D.K., Shadel, G.S., Ladiges, W., et al. (2010). Targeted expression of catalase to mitochondria prevents age-associated reductions in mitochondrial function and insulin resistance. Cell Metabol. *12*, 668–674. https://doi.org/10.1016/j.cmet.2010.11.004.

128. Shukla, S.K., Liu, W., Sikder, K., Addya, S., Sarkar, A., Wei, Y., and Rafiq, K. (2017). HMGCS2 is a key ketogenic enzyme potentially involved in type 1 diabetes with high cardiovascular risk. Sci. Rep. *7*, 4590–4610. https://doi.org/10.1038/s41598-017-04469-z.

129. Armstrong, J.A., Cash, N.J., Ouyang, Y., Morton, J.C., Chvanov, M., Latawiec, D., Awais, M., Tepikin, A.V., Sutton, R., and Criddle, D.N. (2018). Oxidative stress alters mitochondrial bioenergetics and modifies pancreatic cell death independently of cyclophilin D, resulting in an apoptosis-to-necrosis shift. J. Biol. Chem. *293*, 8032–8047. https://doi.org/10.1074/jbc.RA118.003200.

130. Sakamoto, T., Batmanov, K., Wan, S., Guo, Y., Lai, L., Vega, R.B., and Kelly, D.P. (2022). The nuclear receptor ERR cooperates with the cardiogenic factor GATA4 to orchestrate cardiomyocyte maturation. Nat. Commun. *13*, 1991–2020. https://doi.org/10.1038/s41467-022-29733-3.

131. Sakamoto, T., Matsuura, T.R., Wan, S., Ryba, D.M., Kim, J.U., Won, K.J., Lai, L., Petucci, C., Petrenko, N., Musunuru, K., et al. (2020). A Critical Role for Estrogen-Related Receptor Signaling in Cardiac Maturation. Circ. Res. *126*, 1685–1702. https://doi.org/10.1161/CIRCRESAHA.119.316100.

132. Huss, J.M., Imahashi, K.i., Dufour, C.R., Weinheimer, C.J., Courtois, M., Kovacs, A., Giguère, V., Murphy, E., and Kelly, D.P. (2007). The Nuclear Receptor ERR$\alpha$ Is Required for the Bioenergetic and Functional Adaptation to Cardiac Pressure Overload. Cell Metabol. *6*, 25–37. https://doi.org/10.1016/J.CMET.2007.06.005.

133. Landrum, M.J., Lee, J.M., Benson, M., Brown, G.R., Chao, C., Chitipiralla, S., Gu, B., Hart, J., Hoffman, D., Jang, W., et al. (2018). ClinVar: Improving access to variant interpretations and supporting evidence. Nucleic Acids Res. *46*, D1062–D1067. https://doi.org/10.1093/nar/gkx1153.

134. Olson, E.N. (2006). Gene Regulatory Networks in the Evolution and Development of the Heart. Science *313*, 1922–1927. https://doi.org/10.1126/SCIENCE.1132292.

135. Cui, M., Wang, Z., Bassel-Duby, R., and Olson, E.N. (2018). Genetic and epigenetic regulation of cardiomyocytes in development, regeneration and disease. Devenir *145*, dev171983. https://doi.org/10.1242/dev.171983.

136. Lescroart, F., Chabab, S., Lin, X., Rulands, S., Paulissen, C., Rodolosse, A., Auer, H., Achouri, Y., Dubois, C., Bondue, A., et al. (2014). Early lineage restriction in temporally distinct populations of Mesp1 progenitors during mammalian heart development. Nat. Cell Biol. *16*, 829–840. https://doi.org/10.1038/ncb3024.

137. Bondue, A., Lapouge, G., Paulissen, C., Semeraro, C., Iacovino, M., Kyba, M., and Blanpain, C. (2008). Mesp1 acts as a master regulator of multipotent cardiovascular progenitor specification. Cell Stem Cell *3*, 69–84. https://doi.org/10.1016/J.STEM.2008.06.009.

138. Wu, S.M., Fujiwara, Y., Cibulsky, S.M., Clapham, D.E., Lien, C.L., Schultheiss, T.M., and Orkin, S.H. (2006). Developmental Origin of a Bipotential Myocardial and Smooth Muscle Cell Precursor in the Mammalian Heart. Cell *127*, 1137–1150. https://doi.org/10.1016/j.cell.2006.10.028.

139. Kattman, S.J., Huber, T.L., and Keller, G.M. (2006). Multipotent Flk-1+ Cardiovascular Progenitor Cells Give Rise to the Cardiomyocyte, Endothelial, and Vascular Smooth Muscle Lineages. Dev. Cell *11*, 723–732. https://doi.org/10.1016/j.devcel.2006.10.002.

140. Moretti, A., Caron, L., Nakano, A., Lam, J.T., Bernshausen, A., Chen, Y., Qyang, Y., Bu, L., Sasaki, M., Martin-Puig, S., et al. (2006). Multipotent Embryonic Isl1+ Progenitor Cells Lead to Cardiac, Smooth Muscle, and Endothelial Cell Diversification. Cell *127*, 1151–1165. https://doi.org/10.1016/j.cell.2006.10.029.

141. Laforest, B., Bertrand, N., and Zaffran, S. (2014). Anterior Hox Genes in Cardiac Development and Great Artery Patterning. J. Cardiovasc. Dev. Dis. *1*, 3–13. https://doi.org/10.3390/JCDD1010003.

142. Mahmoud, A.I., Kocabas, F., Muralidhar, S.A., Kimura, W., Koura, A.S., Thet, S., Porrello, E.R., and Sadek, H.A. (2013). Meis1 regulates postnatal cardiomyocyte cell cycle arrest. Nature *497*, 249–253. https://doi.org/10.1038/NATURE12054.

143. Paige, S.L., Thomas, S., Stoick-Cooper, C.L., Wang, H., Maves, L., Sandstrom, R., Pabon, L., Reinecke, H., Pratt, G., Keller, G., et al. (2012). A temporal chromatin signature in human embryonic stem cells identifies regulators of cardiac development. Cell *151*, 221–232. https://doi.org/10.1016/j.cell.2012.08.027.

144. Stankunas, K., Shang, C., Twu, K.Y., Kao, S.C., Jenkins, N.A., Copeland, N.G., Sanyal, M., Selleri, L., Cleary, M.L., and Chang, C.P. (2008). Pbx/Meis deficiencies demonstrate multigenetic origins of congenital heart disease. Circ. Res. *103*, 702–709. https://doi.org/10.1161/CIRCRESAHA.108.175489.

145. Liu, R., Jagannathan, R., Li, F., Lee, J., Balasubramanyam, N., Kim, B.S., Yang, P., Yechoor, V.K., and Moulik, M. (2019). Tead1 is required for perinatal cardiomyocyte proliferation. PLoS One *14*, e212116. https://doi.org/10.1371/journal.pone.0212017.

146. Han, Z., Yu, Y., Cai, B., Xu, Z., Bao, Z., Zhang, Y., Bamba, D., Ma, W., Gao, X., Yuan, Y., et al. (2020). YAP/TEAD3 signal mediates cardiac lineage commitment of human-induced pluripotent stem cells. J. Cell. Physiol. *235*, 2753–2760. https://doi.org/10.1002/JCP.29179.

147. Chen, Z., Friedrich, G.A., and Soriano, P. (1994). Transcriptional enhancer factor 1 disruption by a retroviral gene trap leads to heart defects and embryonic lethality in mice. Genes Dev. *8*, 2293–2301. https://doi.org/10.1101/gad.8.19.2293.

148. Stewart, A.F., Suzow, J., Kubota, T., Ueyama, T., and Chen, H.H. (1998). Transcription factor RTEF-1 mediates $\alpha$1-adrenergic reactivation of the fetal gene program in cardiac myocytes. Circ. Res. *83*, 43–49. https://doi.org/10.1161/01.RES.83.1.43.

149. Zanconato, F., Forcato, M., Battilana, G., Azzolin, L., Quaranta, E., Bodega, B., Rosato, A., Bicciato, S., Cordenonsi, M., and Piccolo, S. (2015). Genome-wide association between YAP/TAZ/TEAD and AP-1 at enhancers drives oncogenic growth. Nat. Cell Biol. *17*, 1218–1227. https://doi.org/10.1038/ncb3216.

150. Monroe, T.O., Hill, M.C., Morikawa, Y., Leach, J.P., Heallen, T., Cao, S., Krijger, P.H.L., de Laat, W., Wehrens, X.H.T., Rodney, G.G., and Martin, J.F. (2019). YAP Partially Reprograms Chromatin Accessibility to Directly Induce Adult Cardiogenesis In Vivo. Dev. Cell *48*, 765–779.e7. https://doi.org/10.1016/j.devcel.2019.01.017.

151. Ieda, M., Fu, J.D., Delgado-Olguin, P., Vedantham, V., Hayashi, Y., Bruneau, B.G., and Srivastava, D. (2010). Direct reprogramming of fibroblasts into functional cardiomyocytes by defined factors. Cell *142*, 375–386. https://doi.org/10.1016/j.cell.2010.07.002.

152. Song, K., Nam, Y.J., Luo, X., Qi, X., Tan, W., Huang, G.N., Acharya, A., Smith, C.L., Tallquist, M.D., Neilson, E.G., et al. (2012). Heart repair by reprogramming non-myocytes with cardiac transcription factors. Nature *485*, 599–604. https://doi.org/10.1038/nature11139.

153. Qian, L., Huang, Y., Spencer, C.I., Foley, A., Vedantham, V., Liu, L., Conway, S.J., Fu, J.D., and Srivastava, D. (2012). In vivo reprogramming of murine cardiac fibroblasts into induced cardiomyocytes. Nature *485*, 593–598. https://doi.org/10.1038/nature11044.

154. Chung, S., Arrell, D.K., Faustino, R.S., Terzic, A., and Dzeja, P.P. (2010). Glycolytic network restructuring integral to the energetics of embryonic stem cell cardiac differentiation. J. Mol. Cell. Cardiol. *48*, 725–734. https://doi.org/10.1016/J.YJMCC.2009.12.014.

155. Chung, S., Dzeja, P.P., Faustino, R.S., Perez-Terzic, C., Behfar, A., and Terzic, A. (2007). Mitochondrial oxidative metabolism is required for the cardiac differentiation of stem cells. Nat. Clin. Pract. Cardiovasc. Med. *4*, S60–S67. https://doi.org/10.1038/ncpcardio0766.

156. Wang, G., Yang, L., Grishin, D., Rios, X., Ye, L.Y., Hu, Y., Li, K., Zhang, D., Church, G.M., and Pu, W.T. (2017). Efficient, footprint-free human iPSC genome editing by consolidation of Cas9/CRISPR and piggyBac technologies. Nat. Protoc. *12*, 88–103. https://doi.org/10.1038/NPROT.2016.152.

157. Joung, J., Konermann, S., Gootenberg, J.S., Abudayyeh, O.O., Platt, R.J., Brigham, M.D., Sanjana, N.E., and Zhang, F. (2017). Genome-scale CRISPR-Cas9 knockout and transcriptional activation screening. Nat. Protoc. *124*, 828–863. https://doi.org/10.1038/nprot.2017.016.

158. Lin, Z., Zhou, P., Von Gise, A., Gu, F., Ma, Q., Chen, J., Guo, H., Van Gorp, P.R.R., Wang, D.Z., and Pu, W.T. (2015). Pi3kcb Links Hippo-YAP and PI3K-AKT Signaling Pathways to Promote Cardiomyocyte Proliferation and Survival. Circ. Res. *116*, 35–45. https://doi.org/10.1161/CIRCRESAHA.115.304457.

159. Mandegar, M.A., Huebsch, N., Frolov, E.B., Shin, E., Truong, A., Olvera, M.P., Chan, A.H., Miyaoka, Y., Holmes, K., Spencer, C.I., et al. (2016). CRISPR Interference Efficiently Induces Specific and Reversible Gene Silencing in Human iPSCs. Cell Stem Cell *18*, 541–553. https://doi.org/10.1016/J.STEM.2016.01.022.

160. Fellmann, C., Hoffmann, T., Sridhar, V., Hopfgartner, B., Muhar, M., Roth, M., Lai, D.Y., Barbosa, I.A.M., Kwon, J.S., Guan, Y., et al. (2013). An optimized microRNA backbone for effective single-copy RNAi. Cell Rep. *5*, 1704–1713. https://doi.org/10.1016/J.CELREP.2013.11.020.

161. Kent, W.J., Sugnet, C.W., Furey, T.S., Roskin, K.M., Pringle, T.H., Zahler, A.M., and Haussler, D. (2002). The Human Genome Browser at UCSC. Genome Res. *12*, 996–1006. https://doi.org/10.1101/gr.229102.

162. Schindelin, J., Arganda-Carreras, I., Frise, E., Kaynig, V., Longair, M., Pietzsch, T., Preibisch, S., Rueden, C., Saalfeld, S., Schmid, B., et al. (2012). Fiji: an open-source platform for biological-image analysis. Nat. Methods *9*, 676–682. https://doi.org/10.1038/nmeth.2019.

163. McGinnis, C.S., Murrow, L.M., and Gartner, Z.J. (2019). DoubletFinder: Doublet Detection in Single-Cell RNA Sequencing Data Using Artificial Nearest Neighbors. Cell Syst. *8*, 329–337.e4. https://doi.org/10.1016/J.CELS.2019.03.003.

164. Zhang, Y., Liu, T., Meyer, C.A., Eeckhoute, J., Johnson, D.S., Bernstein, B.E., Nusbaum, C., Myers, R.M., Brown, M., Li, W., and Liu, X.S. (2008). Model-based analysis of ChIP-Seq (MACS). Genome Biol. *9*, R137–R139. https://doi.org/10.1186/GB-2008-9-9-R137.

165. Kolberg, L., Raudvere, U., Kuzmin, I., Adler, P., Vilo, J., and Peterson, H. (2023). g:Profiler—interoperable web service for functional enrichment analysis and gene identifier mapping (2023 update). Nucleic Acids Res. *51*, W207–W212. https://doi.org/10.1093/NAR/GKAD347.

166. Shannon, P., Markiel, A., Ozier, O., Baliga, N.S., Wang, J.T., Ramage, D., Amin, N., Schwikowski, B., and Ideker, T. (2003). Cytoscape: A Software Environment for Integrated Models of Biomolecular Interaction Networks. Genome Res. *13*, 2498–2504. https://doi.org/10.1101/GR.1239303.

167. Li, W., Xu, H., Xiao, T., Cong, L., Love, M.I., Zhang, F., Irizarry, R.A., Liu, J.S., Brown, M., and Liu, X.S. (2014). MAGeCK enables robust identification of essential genes from genome-scale CRISPR/Cas9 knockout screens. Genome Biol. *15*, 554. https://doi.org/10.1186/preaccept-1316450832143458.

168. Andrews, S. (2010). FastQC: A Quality Control Tool for High Throughput Sequence Data. http://www.bioinformatics.babraham.ac.uk/projects/fastqc/%0A%0A.

169. Dobin, A., Davis, C.A., Schlesinger, F., Drenkow, J., Zaleski, C., Jha, S., Batut, P., Chaisson, M., and Gingeras, T.R. (2013). STAR: ultrafast universal RNA-seq aligner. Bioinformatics *29*, 15–21. https://doi.org/10.1093/BIOINFORMATICS/BTS635.

170. Love, M.I., Huber, W., and Anders, S. (2014). Moderated estimation of fold change and dispersion for RNA-seq data with DESeq2. Genome Biol. *15*, 550–621. https://doi.org/10.1186/S13059-014-0550-8.

171. Liao, Y., Smyth, G.K., and Shi, W. (2014). Sequence analysis featureCounts: an efficient general purpose program for assigning sequence reads to genomic features. Bioinformatics *30*, 923–930. https://doi.org/10.1093/bioinformatics/btt656.

172. Wickham, H. (2016). ggplot2: Elegant Graphics for Data Analysis.

173. Robinson, M.D., McCarthy, D.J., and Smyth, G.K. (2010). edgeR: a Bioconductor package for differential expression analysis of digital gene expression data. Bioinformatics *26*, 139–140. https://doi.org/10.1093/BIOINFORMATICS/BTP616.

174. Blighe, K., Rana, S., and Lewis, M. (2018). EnhancedVolcano: Publication-ready volcano plots with enhanced colouring and labeling.

175. Szklarczyk, D., Franceschini, A., Wyder, S., Forslund, K., Heller, D., Huerta-Cepas, J., Simonovic, M., Roth, A., Santos, A., Tsafou, K.P., et al. (2015). STRING v10: protein–protein interaction networks, integrated over the tree of life. Nucleic Acids Res. *43*, D447–D452. https://doi.org/10.1093/NAR/GKU1003.

176. Veevers, J., Farah, E.N., Corselli, M., Witty, A.D., Palomares, K., Vidal, J.G., Emre, N., Carson, C.T., Ouyang, K., Liu, C., et al. (2018). Cell-Surface Marker Signature for Enrichment of Ventricular Cardiomyocytes Derived from Human Embryonic Stem Cells. Stem Cell Rep. *11*, 828–841. https://doi.org/10.1016/j.stemcr.2018.07.007.

177. Neudegger, T., Verghese, J., Hayer-Hartl, M., Hartl, F.U., and Bracher, A. (2016). Structure of human heat-shock transcription factor 1 in complex with DNA. Nat. Struct. Mol. Biol. *23*, 140–146. https://doi.org/10.1038/nsmb.3149.

178. Deacon, D.C., Happe, C.L., Chen, C., Tedeschi, N., Manso, A.M., Li, T., Dalton, N.D., Peng, Q., Farah, E.N., Gu, Y., et al. (2019). Combinatorial interactions of genetic variants in human cardiomyopathy. Nat. Biomed. Eng. *3*, 147–157. https://doi.org/10.1038/s41551-019-0348-9.

179. Butler, A., Hoffman, P., Smibert, P., Papalexi, E., and Satija, R. (2018). Integrating single-cell transcriptomic data across different conditions, technologies, and species. Nat. Biotechnol. *36*, 411–420. https://doi.org/10.1038/nbt.4096.

180. Fornes, O., Castro-Mondragon, J.A., Khan, A., Van Der Lee, R., Zhang, X., Richmond, P.A., Modi, B.P., Correard, S., Gheorghe, M., Baranašić,

D., et al. (2020). JASPAR 2020: update of the open-access database of transcription factor binding profiles. Nucleic Acids Res. *48*, 87–92. https://doi.org/10.1093/nar/gkz1001.

181. Zhou, Y., Liu, Z., Welch, J.D., Gao, X., Wang, L., Garbutt, T., Keepers, B., Ma, H., Prins, J.F., Shen, W., et al. (2019). Single-Cell Transcriptomic Analyses of Cell Fate Transitions during Human Cardiac Reprogramming. Cell Stem Cell *25*, 149–164.e9. https://doi.org/10.1016/j.stem.2019.05.020.

182. Bakshi, A., Zhu, Z., Vinkhuyzen, A.A.E., Hill, W.D., McRae, A.F., Visscher, P.M., and Yang, J. (2016). Fast set-based association analysis using summary data from GWAS identifies novel gene loci for human complex traits. Sci. Rep. *6*, 32894–32899. https://doi.org/10.1038/srep32894.

183. Cuellar-Partida, G., Lundberg, M., Kho, P.F., D'Urso, S., Gutierrez-Mondragon, L.F., and Hwang, L.-D. (2019). Complex-Traits Genetics Virtual Lab: A community-driven web platform for post-GWAS analyses. Preprint at bioRxiv. https://doi.org/10.1101/518027.

## STAR★METHODS

### KEY RESOURCES TABLE

| REAGENT or RESOURCE | SOURCE | IDENTIFIER |
|---|---|---|
| Antibodies | | |
| Alexa Fluor® 647 Anti-mouse/human Ki-67 | BioLegend | Cat# 151206; RRID: AB_2566801 |
| Alexa Fluor® 647 Mouse Anti-Cardiac Troponin T | BD Biosciences | Cat# 565744; RRID: AB_2739341 |
| Recombinant Anti-HSF1 antibody | Abcam | Cat# ab52757; RRID: AB_880518 |
| GAPDH Antibody | Santa Cruz Biotechnology | Cat# sc-25778; RRID: AB_10167668 |
| N-cad Mouse Monoclonal Antibody | Invitrogen | Cat# MA1-91128; RRID: AB_1958717 |
| Cx43 Rabbit Polyclonal Antibody | Invitrogen | Cat# 71–0700; RRID: AB_88403 |
| Anti-Cardiac Troponin T Mouse Antibody | Abcam | Cat# ab8295; RRID: AB_306445 |
| Alexa Fluor 633 Anti-Rabbit | Invitrogen | Cat# A-21072; RRID: AB_2535733 |
| Alexa Fluor 488 Anti-Mouse | Jackson Laboratories | Cat# 715-545-150; RRID: AB_2340846 |
| Alexa Fluor 680 Anti-Mouse | Invitrogen | Cat# A10038; RRID: AB_2534014 |
| Bacterial and virus strains | | |
| Stable Competent E. coli | New England Biolabs | Cat# C3040H |
| Biological samples | | |
| Human fetal heart samples: 15 PCW | UC San Diego Perinatal Biorepository's Developmental Biology Resource (DBR) | N/A |
| Chemicals, peptides, and recombinant proteins | | |
| ROCK inhibitor Y27632 | Tocris | Cat# 1254 |
| CHIR-99021 | Tocris | Cat# 4423 |
| IWP-2 | Tocris | Cat# 3533 |
| poly(2-hydroxyethyl methacrylate) | Sigma-Aldrich | Cat# P3932-10G |
| L-Glutamine | ThermoFisher | Cat# 25030081 |
| 1-Thioglycerol | ThermoFisher | Cat# A18948.30 |
| L-Ascorbic Acid | ThermoFisher | Cat# A15613.22 |
| Human BMP-4 Recombinant Protein | ThermoFisher | Cat# PHC9531 |
| Transferrin | Sigma-Aldrich | Cat# T3705 |
| FGF-basic | PeproTech | Cat# 100-18B |
| Activin A | R&D Systems | Cat# 338-AC |
| SB-431542 | Sigma-Aldrich | Cat# S4317 |
| DAPI | Thermo Fisher Scientific | Cat# D1306 |
| Collagenase, Type IV, powder | Gibco | Cat# 17104019 |
| Hoescht | ThermoFisher | Cat# 62249 |
| ProLong Glass Antifade Mountant | Invitrogen | Cat# P36980 |
| Fluo-4 a.m. ester | Biotium | Cat# 50018 |
| CellROX$^{TM}$ Deep Red Reagent | Invitrogen | Cat# C10422 |
| Tetramethylrhodamine ethyl ester | ThermoFisher Scientific | Cat# T669 |
| Ethidium Homodimer-1 (EthD-1) | ThermoFisher | Cat# E1169 |
| Cas9 protein (for KO generation) | New England Biolabs | Cat# M0386S |
| Geltrex | ThermoFisher | Cat# A1413301 |
| 16% Formaldehyde (w/v) | Thermo Scientific | Cat# 28908 |
| TRIzol Reagent | Invitrogen | Cat# 15596026 |
| Triton X-100 | MP Biomedicals | Cat# 807426 |
| Oligomycin | EMD Millipore | Cat# 495455 |
| 2,4-Dinitrophenol | Sigma Aldrich | Cat# D198501 |

(*Continued on next page*)

*Continued*

| REAGENT or RESOURCE | SOURCE | IDENTIFIER |
|---|---|---|
| Antimycin A | Sigma Aldrich | Cat# A8674 |
| Rotenone | Sigma Aldrich | Cat# R8875 |
| **Critical commercial assays** | | |
| PureLink™ Genomic DNA Mini Kit | Invitrogen | Cat# K182001 |
| QuickExtract DNA Extraction Kit | LGC Biosearch Technologies | Cat# SS00035-D2 |
| Direct-zol RNA Miniprep Kits | Zymo Research | Cat# R2051 |
| **Deposited data** | | |
| Images and Gels | This paper; Mendeley data | Mendeley Data: https://data.mendeley.com/datasets/gkzw2szmzw/2 |
| scRNA-seq/snATAC-seq for human fetal heart samples and scRNA-seq/snATAC-seq for *in vitro* cardiomyocyte differentiations visualization | This paper | https://cells.ucsc.edu/?ds=heart-development |
| scRNA-seq and snATAC-seq for human fetal heart samples: 15 PCW | This paper | Raw sequencing data are available from dbGAP under accession number (dbGAP: phs002031 and dbGAP: phs003473). |
| scRNA-seq for *in vitro* cardiomyocyte differentiations | This paper | Raw sequencing data are available from CIRM CESCG (https://cirm.ucsc.edu) under accession number (chiCardiomyocyte1) |
| snATAC-seq for *in vitro* cardiomyocyte differentiations | This paper | Raw sequencing data are available from GEO under SuperSeries GEO: GSE245499 and SubSeries GEO: GSE245498 https://www.ncbi.nlm.nih.gov/geo/query/acc.cgi?acc=GSE245499 |
| CRISPR/Cas9 TF KO Screen | This paper | Raw sequencing data are available from GEO under SuperSeries GEO: GSE245499 and SubSeries GEO: GSE245496 https://www.ncbi.nlm.nih.gov/geo/query/acc.cgi?acc=GSE245499 |
| HSF1 Bulk RNA-seq data | This paper | Raw sequencing data are available from GEO under SuperSeries GEO: GSE245499 and SubSeries GEO: GSE245497 https://www.ncbi.nlm.nih.gov/geo/query/acc.cgi?acc=GSE245499 |
| **Experimental models: Cell lines** | | |
| HEK293T | Takara | Cat# 632180 |
| H9 MYL2-H2B-GFP *TNNT2*:NLS-mKATE2 | This paper | N/A |
| H9-hTnnT2-pGZ-D2 | WiCell | N/A |
| **Oligonucleotides** | | |
| *HSF1* knockout oligonucleotides; see Table S6 | This paper | N/A |
| Primers for RNA expression and DNA copy number quantification; see Table S6 | This paper | N/A |
| **Recombinant DNA** | | |
| CRISPR/Cas9 TF library | Zhang et al.[108] | Addgene #162275 |
| *TREG*:Cas9 Piggybac | Wang et al.[156] | N/A |
| PB-*TNNT2*:NLS-mKATE2-T2A-BsdR | This paper | N/A |
| lentiMPH v2 | Joung et al.[157] | Addgene #89308 |
| Piggybac plasmid | Laboratory of Karl Willert | #pcsj532 |
| Human-optimized PB transposase (pcsj533) | Laboratory of Karl Willert | #pcsj533 |
| Synthesized *TNNT2* promoter | Lin et al.[158] | N/A |
| pgRNA-CKB66 | Mandegar et al.[159] | Addgene #73501 |
| PCR-amplified PGK from RT3GEPIR | Fellmann et al.[160] | Addgene #111169 |

(*Continued on next page*)

*Continued*

| REAGENT or RESOURCE | SOURCE | IDENTIFIER |
|---|---|---|
| pMD2B | gift from Didier Trono | Addgene #12259 |
| psPAX2 | gift from Didier Trono | Addgene #12260 |
| **Software and algorithms** | | |
| Knockout Guide Design Tool | Synthego | https://design.synthego.com/#/ |
| UCSC Genome Browser | Kent et al.[161] | http://genome.ucsc.edu |
| CellRanger v3.0.1 | 10X Genomics Inc. | http://software.10xgenomics.com/single-cell/overview/welcome |
| Fiji version 2.1.0/1.53c | Schindelin et al.[162] | https://imagej.net/software/fiji/ |
| GraphPad Prism | GraphPad | https://www.graphpad.com/scientific-software/prism/ |
| Seurat v4.0.1 | Hao et al.[96] | https://satijalab.org/seurat/ |
| DoubletFinder | McGinnis et al.[163] | https://github.com/chris-mcginnis-ucsf/DoubletFinder |
| ArchR | Granja et al.[97] | https://www.archrproject.com/ |
| MACS2 version 2.2.7.1 | Zhang et al.[164] | https://github.com/macs3-project/MACS |
| Pando (v1.0.0) | Fleck et al.[68] | https://github.com/quadbio/Pando |
| g:Profiler | Kolberg et al.[165] | https://biit.cs.ut.ee/gprofiler/gost |
| URD v.1.1.1 | Farrell et al.[103] | https://github.com/farrellja/URD |
| Cytoscape version 3.7.2 | Shannon et al.[166] | https://cytoscape.org/ |
| MaGeCK | Li et al.[167] | https://sourceforge.net/p/mageck/wiki/Home/ |
| FASTQC | Andrews[168] | https://www.bioinformatics.babraham.ac.uk/projects/fastqc/ |
| STAR aligner | Dobin et al.[169] | https://github.com/alexdobin/STAR |
| DESeq2 | Love et al.[170] | https://www.bioconductor.org/packages/release/bioc/html/DESeq2.html |
| featureCounts | Liao et al.[171] | https://subread.sourceforge.net/featureCounts.html |
| ggplot2 | Wickham[172] | https://ggplot2.tidyverse.org/index.html |
| edgeR | Robinson et al.[173] | https://bioconductor.org/packages/release/bioc/html/edgeR.html |
| EnhancedVolcano | Blighe et al.[174] | https://github.com/kevinblighe/EnhancedVolcano |
| STRING database | Szklarczyk et al.[175] | https://string-db.org/ |
| FLOWJO 10.7.1 | BD Biosciences | https://www.flowjo.com/ |
| Sony SH800/MA900 Cell Sorter Software | Sony | https://www.sonybiotechnology.com/us/instruments/ma900-multi-application-cell-sorter/ |
| CFX Manager version 3.1 Software | Bio-Rad | https://www.bio-rad.com/en-us/sku/1845000-cfx-manager-software?ID=1845000 |
| Seahorse Wave Software | Agilent | https://www.agilent.com/en/product/cell-analysis/real-time-cell-metabolic-analysis/xf-software/seahorse-wave-desktop-software-740897 |
| **Other** | | |
| MATLAB script for calcium imaging analysis | This paper | https://doi.org/10.5281/zenodo.13798843 |

## EXPERIMENTAL MODEL AND STUDY PARTICIPANT DETAILS

### HEK293T cells

HEK293T cells were cultured in DMEM (Gibco) supplemented with 10% FBS at 37°C, 5% CO2. HEK293T were maintained by dissociation into single cells at 70–80% confluency with TrypLE (Gibco) and seeded at a dilution of 1:10 in DMEM with 10% FBS.

### hPSCs

For the CRISPR/Cas9 screen, an engineered *TREG3*:Cas9 Piggybac (PB) plasmid (generous gift from William Pu[156]) was jointly transfected with a *TNNT2:*NLS-mKATE2-T2A-BsdR PB plasmid into H9 hPSCs with a MYL2-H2B-GFP bacterial artificial chromosome.[176]

To generate the PB-*TNNT2:*NLS-mKATE2-T2A-BsdR plasmid, we used the PB plasmid pcsj532 (generous gift from Karl Willert, UCSD) and used Gibson assembly (SGI, GA1200) to clone in a synthesized *TNNT2* promoter[158] (Integrated DNA Technologies), PCR-amplified NLS-mKATE2-T2A-BsdR (with polyA) from pgRNA-CKB66[159] (generous gift from Bruce Conklin, Gladstone), PCR-amplified PGK from RT3GEPIR[160] (generous gift from Johannes Zuber, IMP, Austria), and PCR-amplified HygroR from lentiMPH v2[157] (generous gift from Feng Zhang). All four components were assembled using one Gibson assembly reaction with pcsj532 digested using NheI (NEB R3131L). The PB-*TREG3*:Cas9 plasmid was also modified by changing out the PuroR to BsdR in a similar method as described above. H9 hPSCs were jointly transfected using Lipofectamine STEM Reagent (Invitrogen STEM00015) with the PB-*TREG3:Cas9*, PB-*TNNT2:*NLS-mKATE2-T2A-BsdR, and a plasmid expressing a human-optimized PB transposase (pcsj533, generous gift from Karl Willert, UCSD) to integrate the PB. Two days after transfection, the cells were selected using 1 μg/mL blasticidin and 10 μg/mL hygromycin. The surviving cell pool behaved similarly to the parental line in terms of proliferation and differentiation. Protocols were approved by #190561 (Institutional Review Board) at the University of California, San Diego.

For the 2D and 3D hPSC-CM experiments, an H9 hPSC line with a MYL2-H2B-GFP bacterial artificial chromosome and *TNNT2:*NLS-mKATE2 reporter was used. For the *in vitro* single-cell and *HSF1* KO studies, the H9-*hTnnT2*-pGZ-D2 line (*TNNT2:*GFP hPSC-CM reporter line) from WiCell was utilized.

hPSC lines were cultured in mTeSR Plus Medium (Stem Cell Technologies) on 1:100 diluted Geltrex (Gibco) coated plates at 37°C, 5% CO2. Lines were maintained by dissociating into single cells at 70% confluency with TrypLE (Gibco), quenching in RPMI-1640 with 10% FBS, centrifuging at 200 g for 5 min to remove the dissociation reagent, and seeding at a dilution of 1:10 in mTeSR Plus Medium supplemented with 4 μM ROCK inhibitor Y27632 (Tocris) onto Geltrex coated plates. After 24 h, the medium was replaced with mTeSR Plus Medium without ROCK inhibitor with daily medium changes thereafter.

### Generation of an H9 HSF1 KO cell line

*HSF1*-targeted single guide RNAs (sgRNAs) were designed to target the human *HSF1* DNA binding domain located within exons 2–4.[177] sgRNAs were selected based on on-target and off-target prediction scores from Synthego (https://design.synthego.com/#/) and as displayed in the UCSC genome browser (http://genome.ucsc.edu).[161] Four sgRNAs were ordered from Synthego targeting exon 4 with two sgRNAs on the 5′ end of the exon and two sgRNAs on the 3′ end of the exon. H9-*hTnnT2*-pGZ-D2 cells plated at a density of 250,000 cells were transfected with the following mix in four combinations for each of the sgRNA pairings (e.g., 5′ sgRNA 1 and 3′ sgRNA 1, etc.). In tube 1, 1.6 μg each from one of two 5′ and 3′ sgRNAs and 1.2 μL of 20 μM Cas9 protein was added to 50 μL Opti-MEM (Gibco). In tube 2, 4 μL lipofectamine 2000 was added to 50 μL Opti-MEM. Tubes were mixed and incubated for 10 min at room temperature, and added to H9 cells dropwise.

Two days after transfection, cells with each of the sgRNA pairings were individually split into two groups: one group was used for KO efficiency assessment and another group was seeded at a density of 2,000 cells in a 10 cm dish for clone selection. KO efficiency assessment was performed by purifying the genomic DNA according to the PureLink Genomic DNA Mini Kit (Invitrogen), conducting PCR (ThermoFisher, Platinum SuperFi PCR Master Mix) by amplifying the knocked-out region, and running a 2% agarose gel on the PCR product for the ratio of smaller, or KO DNA, to larger, or wild type DNA, fragment sizes. sgRNA pairings 5′ sgRNA 1 + 3′ sgRNA 1 and 5′ sgRNA 2 + 3′ sgRNA 1 were selected for having the highest pooled KO efficiency.

Colonies for the selected sgRNA pairings were expanded for one week and individually scraped into a 96-well plate with mTeSR supplemented with 4 μM ROCK inhibitor. Once 90% confluent, cells were dissociated using versene (Gibco) and split into two 96-well plates. One plate was used for homozygous KO identification by extracting the genomic DNA using a QuickExtract kit (LGC Biosearch Technologies), conducting PCR (EmeraldAmp PCR Master Mix, Takara) by amplifying the knocked-out region, and running a 2% agarose gel on the PCR product for a smaller fragment size. Of the clones, approximately 50% were homozygous and 25% were heterozygous. Once these clones were identified, the other 96-well plate was used to expand, sequence, and freeze the homozygous clones until differentiation. DNA sequencing was performed by purifying the DNA according to the PureLink Genomic DNA Mini Kit (Invitrogen) and submitting the samples for Sanger sequencing (Eton Biosciences).

### Human fetal heart tissues

De-identified tissue samples were collected with previous patient consent in strict observance of the legal and institutional ethical regulations. Protocols were approved by #101021 (Institutional Review Board) at the University of California, San Diego.

## METHOD DETAILS

### Experimental procedures

#### *Differentiation of hPSCs into CMs in 2D- and 3D-hPSC systems*

H9 hPSCs were differentiated into 2D and 3D hPSC-CM systems following predefined protocols.[80,81] Briefly, in the 2D-hPSC system, hPSCs were seeded at a range of densities from 1-2x$10^5$ cells per well in a 12-well plate (day −2) and fed with mTeSR Plus Medium for 2 days. At this time (day 0), cells were treated with RPMI-1640 medium with B27 Supplement without insulin (RPMI B27-; Gibco)

supplemented with 10 μM CHIR-99021 (CHIR; Tocris). 24 h later (day 1), the medium was changed to RPMI B27-, and 48 h later (day 3) the cells were treated with RPMI B27- supplemented with 5 μM IWP-2 (Tocris) for 48 h. 2 days later (day 5), the medium was changed to RPMI B27-, and on day 7 until dissociation, the medium was changed every 3 days with RPMI with B27 Supplement with insulin (RPMI B27+). All functional analyses were performed after 25 days of differentiation.

In the 3D-hPSC system, hPSCs were seeded at a density of $5x10^5$ per well in a 6-well and fed with mTeSR Plus Medium until 95–100% confluency was achieved (~3 days, day 0). At day 0, plates were coated with 5% poly(2-hydroxyethyl methacrylate) (Sigma-Aldrich) to prevent cell attachment, and cells were dissociated as aggregates (“EBs”), spun down, and resuspended in StemPro-34 SFM (ThermoFisher) medium supplemented with 2mM L-Glutamine (ThermoFisher), 1-Thioglycerol (ThermoFisher), and 64 μg/mL L-Ascorbic Acid (ThermoFisher) termed “SP base” with 1:250 Geltrex (ThermoFisher), 10 μM ROCK inhibitor, 1 ng/mL BMP4 (ThermoFisher), and 50 mg/mL Transferrin (Sigma-Aldrich). 24 h later (day 1), EBs were spun down and resuspended in SP base media with 50 mg/mL Transferrin, 5 ng/mL FGF-basic (PeproTech), 8–10 ng/mL BMP4, and 10 ng/mL Activin A (ActA; R&D Systems). 3 days later (day 4), EBs were spun down and resuspended in SP base media with 50 mg/mL Transferrin, 15 mM SB-431542 (Sigma-Aldrich), and 5 μM IWP2. 2 days later (day 6), EBs were allowed to settle in the bottom of the wells and media was supplemented with SP base media with 50 mg/mL Transferrin, and at day 8 on, media was supplemented with only SP base media. All functional analyses were performed at 25 days of differentiation.

### Collections for scRNA-seq and snATAC-seq

For the *in vitro* single-cell studies, the hPSC H9-*hTnnT2*-pGZ-TD2 line was differentiated into CMs and their corresponding developmental stages using the two protocols discussed above, with differentiation efficiency measured using flow cytometry as done previously.[95] Cells from hPSC, mesoderm, cardiac mesoderm, and CM stages were dissociated as done previously[95] and processed fresh for droplet-based scRNA-seq and snATAC-seq. Dissociated cells were stained with DAPI (Thermo Fisher Scientific) to identify viable cells (DAPI-negative). In total, 100,000 cells, for scRNA-seq, and 500,000 cells, for snATAC-seq, were sorted and collected using a Sony SH800 sorter ($n = 2$).

For the *in vivo* human fetal heart single-cell dissociation and collection, tissue samples were collected in buffer containing 10 mM HEPES pH 7.8, 130 mM NaCl, 5 mM KCl, 10 mM Glucose, 10 mM BDM, 10 mM Taurine, 1 mM EDTA, and 0.5 mM $NaH_2PO_4$, and overall morphology was checked under a stereotaxic dissection microscope (Leica). Tissue samples from eight hearts were further cut into small pieces and enzymatically digested by incubating with Collagenase Type IV (Gibco) and Accutase (ThermoFisher) at 37°C for 60 min. After removing the dissociation media, cells were resuspended in PBS supplemented with 5% FBS and sorted on a Sony SH800 sorter. Samples were diluted to approximately 1,000 cells per μL before processing for scRNA-seq.

For scRNA-seq, single-cell droplet libraries using the cell suspensions from the Sony SH800 sorter were prepared according to the manufacturer’s instructions using the 10X Genomics Chromium controller, Chromium Single Cell 3′ Library, Gel Bead Kit v2 (PN-120237), and Chromium i7 Multiplex Kit (PN-120262). All libraries were sequenced on the HiSeq 4000 (Illumina) to a mean read depth of at least 65,000 total aligned reads per cell. For snATAC-seq, cells were pelleted using the cell suspensions from the Sony SH800 sorter, and the nuclei were isolated and prepared as described previously[95] for library sequencing. Libraries were sequenced on NextSeq 500 or HiSeq4000 sequencers (Illumina) using custom sequencing primers with the following read lengths: 50 + 10 + 12 + 50 (read 1 + index 1 + index 2 + read 2).

### Flow cytometry

CMs were dissociated into single cells using Collagenase Type IV (Gibco) for 30 min at 37°C, followed by 5 min of Accutase. Dissociation was quenched using RPMI-1640 with 10% FBS, and cells were centrifuged for 5 min at 200 *g*. For *TNNT2* reporter-based flow cytometry, cells were examined without fixation with the *TNNT2*:NLS-mKATE2 or *TNNT2*:GFP reporter. For TNNT2 and Ki-67 antibody-based flow cytometry, cells were fixed in PBS/4% paraformaldehyde with the Alexa Fluor 647 Mouse Anti-Cardiac Troponin T (BD, 1:200, cat# 565744) or Alexa Fluor 647 anti-mouse/human Ki-67 antibody (BioLegend, 1:100, catalog: 151206). Fixed cells were washed and stained in PBS with 5% bovine serum albumin (Sigma) and 0.1% Triton X-100 (MP Biomedicals) with antibodies in the dark for 1 h at room temperature or at 4°C overnight, and then washed twice using PBS. Live and fixed cells were resuspended in PBS with 5% bovine serum albumin and filtered to obtain a single cell suspension for flow cytometry analysis on an MA900 Multi-Application Cell Sorter (Sony) or FACSAria (BD). Data were collected using the Sony software, and processed and analyzed using FlowJo software (BD Biosciences). Percentage of proliferating CMs was calculated by dividing the percentage of Ki-67+ *TNNT2*:GFP+ cells over *TNNT2*:GFP+ cells.

### CRISPR/Cas9 TF KO screen

A comprehensive TF KO library targeting 1,639 TFs from Zhang et al.[108] (Addgene, #162275) was amplified as described[108] in order to gain sufficient sgRNA coverage and distribution across the library. Single-end 150 base pair sequencing was performed using a NovaSeq S4 on the original and amplified libraries, which had high Pearson correlation. To produce virus, HEK293T cells were seeded in a 10 cm dish in DMEM (Gibco) supplemented with 10% FBS and grown to 70–80% confluency. Cells were transfected with the following mix. In tube 1, 15 μg of plasmid DNA, 5 μg pMD2B, and 10 μg psPAX2 were added to Opti-MEM (Gibco) to 500 μL total. In tube 2, 100 μL lipofectamine 2000 was added to 400 μL Opti-MEM. Tubes were mixed and incubated for 10 min at room temperature, and added to HEK293T cells dropwise. Media was changed the following day and virus was collected the following two days by removing the supernatant, centrifuging at 200 g for 5 min, filtering through a 0.45 μM filter, and storing at −80°C until usage.

20 million H9 hPSC *TNNT2:*NLS-mKATE2 and *TREG3*:Cas9 cells were transduced with the pooled lentiviral library at a multiplicity of infection of 0.3. After 4 days of 1 μg/mL puromycin, for selection of transduced cells, and 3 days of 1 μg/mL doxycycline, for Cas9 activation, two replicates of 6 million of the surviving cells were taken as day 0 controls, and the rest of the cells were maintained for additional replicates or differentiated using 2D- and 3D-hPSC differentiation protocols. Three biological replicates were differentiated and sorted into *TNNT2*+ and *TNNT2*-cells amounting to 6 million cells total. Genomic DNA purification was performed using PureLink Genomic DNA Mini Kit (Invitrogen), and two rounds of PCR were performed for sgRNA amplification and addition of indexing primers (Table S6). Single-end 150 base pair sequencing was performed using a NovaSeq S4 (Illumina). Each library was sequenced to achieve ~500x average coverage over the CRISPR library.

### Gene expression and mtDNA copy number quantification

RNA was extracted using TRIzol (Invitrogen) following the manufacturer's protocol and purified using a Direct-zol RNA Miniprep Kit (Zymo Research). cDNA was transcribed from 1 μg of RNA using iScript Supermix (Bio-Rad). Genomic DNA purification was performed using PureLink Genomic DNA Mini Kit (Invitrogen). Gene expression or DNA copy number was analyzed using Power SYBR Green Master Mix (ThermoFisher Scientific) at 10 ng concentration cDNA or 15 ng DNA and run on a CFX Connect qPCR machine (Bio-Rad) using CFX Manager version 3.1 software. Relative expression levels of each gene were determined by normalizing expression levels to *TBP* or to *TBP* and then control. Relative copy number of mitochondrial DNA (*MT-TL1*) was determined by normalizing copy number to a nuclear DNA (*MYH7*). Primer sequences are listed in Table S6.

### Western blot

To confirm *HSF1* KO in clonal hPSC lines, lysates were prepared using NuPAGE LDS sample buffer (Invitrogen) and run on a 4%–12% NuPAGE gradient gel (Invitrogen) for western analysis. Gels were transferred using standard procedures.[178] Nitrocellulose membranes were stained with antibodies for HSF1 (1:1,000 dilution; Abcam) and GAPDH (1:1,000 dilution; Santa Cruz Biotechnology) as loading control. After washing, the blot was stained with HRP-linked anti-rabbit IgG. Blot was developed using Clarity ECL (Bio-Rad), imaged using a BioRad ChemiDoc XRS+, and cropped in ImageJ to remove the ladder.

### Immunofluorescent assays

In 2D hPSC-CMs, cells were dissociated and plated at a density of 200,000 cells in a Geltrex-coated glass-bottom chamber slide. 3 days after replating, cells were washed with PBS prior to fixation with 4% PFA in PBS for 10 min at room temperature. In 3D hPSC-CMs, embryoid bodies were washed in DPBS prior to fixation with 4% PFA in PBS for 30 min at room temperature. Embryoid bodies were then washed with PBS twice and stored in 30% sucrose in PBS overnight at 4°C before embedding in optimal cutting temperature (OCT) compound. Embedded cells were then sectioned at 10 μM using a Leica Cryostat (Leica CM3050S) at −20°C, placed on a glass slide, and stored at −20°C until staining was performed. For staining, cells were permeabilized in PBS with 0.25% Triton X-100 for 10 min and blocked for 2 h in blocking buffer (PBS with 0.25% Triton X-100, 5% bovine serum albumin, and 5% normal donkey serum). Cells were incubated in N-cad Mouse Monoclonal Antibody (Invitrogen, 1:200, cat: MA1-91128), Cx43 Rabbit Polyclonal Antibody (Invitrogen, 1:500, cat: 71–0700, lot: WC324579), and/or Anti-Cardiac Troponin T Mouse Antibody (Abcam, 1:200, ab8295) antibodies in blocking buffer overnight at 4°C. Samples were then incubated in Alexa Fluor 633 Anti-Rabbit (with Cx43; Invitrogen, 1:1000, cat: A-21072, lot: 1904421), Alexa Fluor 488 Anti-Mouse (with N-cad; Jackson Laboratories, 1:1000, cat: 715-545-150, lot: 92290), and/or Alexa Fluor 680 Anti-Mouse (with TNNT2; Invitrogen, 1:1000, cat: A10038, lot: 2680407) secondary antibodies or Alexa Fluor 647 anti-mouse/human Ki-67 antibody (BioLegend, 1:100, catalog: 151206) in blocking buffer for 2 h at room temperature. Samples were lastly incubated in Hoescht (ThermoFisher) for 10 min at room temperature, mounted on slides with ProLong Glass Antifade Mountant (Invitrogen), and allowed to dry overnight prior to immunofluorescent imaging. Cells were imaged at 60x using a Nikon T2 confocal microscope. Rod morphology was calculated using N-cad staining by measuring and dividing the long axis by the short axis of each cell in Fiji.[162] N-cad and Cx43 co-localization analysis was performed in Fiji by measuring the fluorescent intensity over a linear space in each channel.

### Calcium imaging

Cells were dissociated and plated at a density of 300,000 cells/dish in a glass-bottom dish. Three days after replating, cells were washed with PBS, treated with 2 μM fluo-4 a.m. ester (Biotium) in RPMI B27+ for 15 min at 37°C, and imaged at 488 nm excitation. Cells were imaged at 60x using a Nikon T2 confocal microscope using the linescanning feature. Linescans were processed using a custom MATLAB script. Source code is available at https://github.com/arholman-ucsd/calcium-imaging-matlab-script/tree/main.

### ROS and mitochondria quantification and visualization

ROS and mitochondria visualization were performed using CellROX Deep Red Reagent (Invitrogen) and tetramethylrhodamine ethyl ester (TMRE) compound (ThermoFisher Scientific), respectively. Cells were dissociated and plated at a density of 300,000 cells in a glass-bottom dish. Three days after replating, cells were washed with PBS, treated with 200 nM TMRE and 5 μM CellROX in RPMI B27+ for 30 min at 37°C, washed twice with PBS, and returned to RPMI B27+ for imaging (CellROX has an absorption/emission maxima at ~644/665 nm, and TMRE has 488 nm excitation 575 nm emission). Cells were imaged at 60x using a Nikon T2 confocal microscope. Representative images were processed using Fiji software and selected by the presence of *TNNT2*:GFP+ cells. ROS and mitochondria content were quantified by measuring the cell area raw intensity of CellROX divided by TMRE and measuring the cell area raw intensity of TMRE divided by cell area, respectively.

### Seahorse analysis

Dissociated cells were plated at 150,000 cells per well in a 96-well microplate (Agilent). Three days post-plating, an XF Cell Mito Stress Test (Agilent; Oligomycin 1.5 μM, 2,4-Dinitrophenol (DNP) 100 μM, Antimycin A and Rotenone 0.5 μM) was performed using

an XFe96 Analyzer. Cell numbers were normalized through cell counting, and resulting data were analyzed using Seahorse Wave Software. Data were represented by subtracting the average of Antimycin A and Rotenone values.

#### *Apoptosis assay and quantification*

CM-specific apoptosis quantification was performed using nuclear EthD-1 (ThermoFisher) for dead cells, cytoplasmic *TNNT2*:GFP for CMs, and nuclear Hoescht for cells. Cells were dissociated and plated at a density of 300,000 cells in a glass-bottom dish. Three days after replating, cells were washed with PBS and treated with 4 μM EthD-1 and 20 μM Hoescht for 30 min at room temperature. Cells were imaged at 405 nm for Hoescht, 488 nm for *TNNT2*:GFP, and 567 nm for EthD-1 emission at 60x using a Nikon T2 confocal microscope. Images were processed using Fiji software where 100 CMs per sample were analyzed for co-localization of Hoescht, EthD-1, and *TNNT2*:GFP (dead CMs) or co-localization of Hoescht and *TNNT2*:GFP without EthD-1 (live CMs). Percentage of CM-specific cell death was quantified by dividing the number of dead CMs by the sum of the number of live and dead CMs.

### Data analysis

#### *Data processing for scRNA-seq*

For the *in vitro* scRNA-seq, following demultiplexing and alignment to Hg38 using CellRanger (v3.0.1 pipeline, 10X Genomics), individual count matrices from both differentiation systems and all timepoints were merged and processed using Seurat (v4.0.1 R package).[179] Initially, quality control filters were used to exclude low quality cells that express more than 7,500 genes (doublets) or less than 1,000 genes and more than 25% mitochondria. Batch correction was performed based on replicates. Principal components were calculated and the top 30 PCs were used for clustering into groups based on the default 0.8 resolution, and UMAP dimensionality reduction was used to visually display the cells. Cellular annotations were assigned to each cluster by using known markers. Differential gene analysis was performed using a $\log_2$ (fold change) value greater than 0.5 and an adjusted $p$-value less than 0.05.

*In vivo* scRNA-seq data processing was performed in a similar fashion to the *in vitro* data. Briefly, after generating the gene-barcode matrix file from Cell Ranger, the individual count matrices were merged using Seurat. Initially, quality control filters were used to exclude low quality cells that express less than 1,000 genes and more than 30% mitochondria. Potential doublets were removed using DoubletFinder,[163] using an anticipated doublet rate of 5%. Gene expression was normalized and the top 3,000 variable genes were detected. Principal components were calculated and the top 50 principal components were used for creating the nearest neighbor graph. The generated nearest neighbor graph was then used for graph-based, semi-unsupervised clustering based on the default 0.8 resolution, and UMAP was used to project the cells into two dimensions. Marker genes were identified using a Wilcoxon rank-sum test for one-versus-all comparisons for each of the cell clusters. Cell identities were assigned to the clusters by cross-referencing their marker genes with known cardiac cell type markers from both human and mouse studies, in addition to *in situ* hybridization data from the literature.[48–50,52] On occasion, a cell cluster would emerge that expressed marker genes representing multiple populations, as well as contained cells with low UMI and gene counts that escaped the first filtering step. These cells were removed from downstream analyses.

#### *Data processing for snATAC-seq*

snATAC-seq data processing and analysis were performed as done previously[95] with additional information described below. The ArchR package was used for processing, analysis, and visualization of the data. The data were filtered for cells $\geq$ 1,000 fragments and a TSS enrichment of 4.

Two biological replicates for the *in vitro* data from day 0 to day 25 from 2D- and 3D-hPSC systems were merged and batch-corrected using Harmony after an iterative latent semantic indexing (LSI) dimensionality reduction. After batch correction, 31 clusters were identified at a resolution of 1.8. The clusters were annotated using known gene markers, resulting in 10 cell populations, and visualized using UMAP. MACS2[164] (version 2.2.7.1) was used to call peaks for each cluster, which was run with default parameters. A reproducible peak set and a peak count matrix per cell was computed after peak calling. The peak count matrix and the Wilcoxon test was used to identify unique differential peaks across clusters ($p$-value <0.05 and $\log_2$ (fold change) > 0). To identify differentially enriched motifs in *cis*-regulatory elements between the 2D- and 3D-hPSC differentiations by day, motif enrichment was used to annotate the peak set using the Jaspar 2020 database.[180] We identified differential marker peaks and then ran motif enrichment on each set of peaks using all peaks as the background ($p$-value <0.05 and $\log_2$ (fold change) > 0).

Two biological replicates for the *in vivo* 15 PCW data were processed similarly for IVS, LA, LV, RA, and RV samples with the same quality-based filtering parameters as above. After batch correction, 23 clusters were identified with a clustering resolution of 0.8 and annotated into 11 cell populations. Peak calling and motif enrichment were calculated the same way as above.

#### *Mapping between RNA and ATAC datasets*

The annotated scRNA-seq data were integrated and label transferred onto the snATAC-seq data via ArchR, which uses a modified version of the transfer by anchors method from Seurat. The predicted gene expression from the scRNA-seq was also integrated as the gene integration matrix. The annotated snATAC-seq data were integrated and label transferred onto the scRNA-seq data via Seurat integration by anchors. The anchors were filtered for only the top scoring anchors between the datasets. The predicted gene scores, motif z-scores, and peaks from the snATAC-seq were also transferred.

### Label transfer from developmental atlas datasets

We combined Tyser et al. 2021,[98] which utilizes early human gastrulation samples, and Farah et al. 2024,[99] which utilizes early human heart samples, as reference datasets to label transfer onto our combined 2D/3D scRNA-seq dataset. The label transfer was done using Seurat after finding transfer anchors between the two datasets and projecting the UMAP space. Low mapping scores below the bottom quartile threshold were filtered out.

### Gene ontology

To identify biological processes associated with gene datasets, the R package 'g:Profiler'[165] was used using either the single-query or multi-query settings. -Log10(*p*-values) or adjusted *p*-values were shown for GO enrichment. Significance was either represented through a dot plot made using ggplot2 or as a numerical value. To identify GO terms associated with differential motifs and associated transcription factors, STRING database[175] biological process was used to identify the most enriched (highest strength) GO terms with associated false discovery rates. False discovery rate was shown for GO enrichment as a numerical value.

### Pseudotime trajectory analysis

Pseudotime and cell trajectory analyses were performed with the URD package (v.1.1.1). The scRNA-seq data from day 0 through 25 including both differentiation methods were processed in Seurat as described above. A 50,000 cell downsampling was used in creating and calculating the URD trajectory with a k-nearest neighbors value of 1,000 and 50,000 random walk simulations. The hPSC cell population was set as 'root' and the 5 cell populations present at day 25 (2D hPSC-CM, 3D hPSC-CM, MP, VE, and Endoderm) were set as 'tip' cells. The resulting pseudotime was utilized in the GRN of the CM lineage cell populations (mesendoderm, LPM, cardiac mesoderm, CM) by determining the expression-weighted pseudotime of each respective TF.

### Gene regulatory network analysis

The gene regulatory networks were constructed using Pando[68] (v1.0.0) on the snATAC-seq data with scRNA-seq integration. The CM lineage cell populations (mesendoderm, LPM, cardiac mesoderm, CM) for the combined 2D- and 3D-hPSC systems, 2D-hPSC system, and the 3D-hPSC system were used to infer the *in vitro* GRNs. The *in vivo* 15 PCW fetal CMs were used to infer the *in vivo* GRN. The standard Pando pipeline steps were performed: 1) initiate the GRN, 2) find TF binding sites, 3) infer the GRN, and 4) extract modules. GRNs were visualized with the gene correlation UMAP embedding or Cytoscape.[166]

The 2D vs. 3D hPSC-CM branch-specific GRN was constructed by filtering the CM lineage GRN by the differential TFs (by both gene expression and motif utilization enrichment) between pre-split and post-split as well as 2D- and 3D-hPSC system branches from the URD trajectory. The 2D-vs. 3D-hPSC system branch-specific TFs were determined by quantifying the number of differentially expressed genes between 2D- and 3D-hPSC system branches for each TF.

### Data processing for CRISPR/Cas9 TF KO screen

The MaGeCK pipeline[167] was used for the identification of essential genes using the 'MLE' tool and differential analysis of read abundances between CMs and non-CMs, as compared to day 0. We defined TFs promoting CM differentiation as those with a positive non-CM *Z* score and negative CM *Z* score, and conversely, we defined TFs blocking CM differentiation as those with a negative non-CM *Z* score and positive CM *Z* score. TF GO analysis was performed using STRING database biological process as described above.

### Bulk RNA-seq

RNA-seq was performed as previously published.[95] For *HSF1* KO and control RNA-seq, total RNA from 3D day 25 cells was extracted using TRIzol (Invitrogen) and purified using the Direct-zol RNA Miniprep Kit (Zymo Research) from three independent replicates. Bulk RNA-seq was performed by the Institute for Genomic Medicine at UC San Diego using the Illumina Total RNA Ribodepleted Prep. Pair-end 100 base pair sequencing was performed using a NovaSeq S4 (Illumina). Quality of sequencing data was assessed using FASTQC.[168] Reads were aligned to Hg38 using STAR[169] and counted using featureCounts.[171] DESeq2[170] was used to identify differentially expressed genes from raw read counts comparing control and KO with biological replicates as a covariate. Top differentially expressed genes were filtered with a $\log_2$(fold change) filter of 0.5 and adjusted *p*-value filter of 0.05 to construct a volcano plot,[174] and were used for GO term analysis using g:Profiler as previously described. Normalization of sequencing data into $\log_2$(counts per million) was completed with edgeR.[173]

### CM maturation index

A developing human heart dataset containing samples from 9, 11, 13, and 15 PCW from Farah et al. 2024[99] was first partitioned for CM (aCM, vCM, and ncCM) cell populations. Differentially expressed genes were identified between 9 and 15 PCW CM cell populations, and subsequently centroids were calculated based on these genes, as done previously.[181] For each cell, including cells from 9 to 15 PCW CM cell populations from Farah et al. 2024,[99] and 25-day 2D and 3D hPSC-CMs from our combined 2D/3D-hPSC system dataset, gene expression was weighted based on the calculated centroids to determine the CM maturation on a per cell basis, representing the position of a cell along the 9 to 15 PCW axis.

### Association between HSF1 GRN and cardiac traits in the general human population

Gene-based tests on GWAS summary data from ten cardiac traits were performed using fastBAT[182] implemented in the Complex-Traits Genetics Virtual Lab[183] and filtered for significant genes ($p < 0.05$). A Fisher's Exact Test was then used to determine enrichment for the cardiac trait-associated genes within the *HSF1* GRNs based on a null hypothesis of the number of cardiac trait-associated genes as stated below out of 24,273 genes in the GWAS summary data. There were 375 associated genes with CHD based on previously published datasets,[67] and 1572 with "Ventricular Rate", 1729 with "QRS duration", 1983 with "Pulse wave peak to peak time", 1379 with

"P duration", 2422 with "ECG, heart rate", 14468 with "Basal metabolic rate", 894 with "Cardiomyopathy(hypertrophic, obstructive) (HCM) (All Biobanks)", 2503 with "Diagnoses - main ICD10: I48 Atrial fibrillation and flutter", 1575 with "Death due to cardiac causes", and 1722 with "Heart failure" based on GWAS data.

## QUANTIFICATION AND STATISTICAL ANALYSIS

Unless otherwise noted, all data are represented as mean +/− standard error of mean (SEM) and obtained from independent tissue samples or differentiations. Except for figures pertaining to single-cell or bulk RNA-seq studies where graphs made primarily using ggplot2,[172] all graphs and analyses were executed in Prism 9 with statistical significance as follows: $p < 0.05$. *$p < 0.05$, **$p < 0.01$, ***$p < 0.001$, ****$p < 0.0001$. The t-Student test (unpaired, two-tailed) was utilized for two group comparisons. Sample sizes were not predetermined, and the experiments were not blinded.